Article:
Planavsky, NJ, Fakhraee, M, Bolton, EW et al. (4 more authors) (2022) On Carbon Burial and Net Primary Production Through Earth's History. American Journal of Science, 322 (3). pp. 413-460. ISSN 0002-9599

https://doi.org/10.2475/03.2022.01

On Carbon Burial and Net Primary Production Through Earth's History

Noah J. Planavsky[1]*, Mojtaba Fakhraee[1,2], Edward W. Bolton[1], Christopher T. Reinhard[2], Terry T. Isson[3], Shuang Zhang[4], and Benjamin J.W. Mills[5]

[1]Department of Earth and Planetary Sciences, Yale University, CT, USA

[2]School of Earth & Atmospheric Sciences, Georgia Institute of Technology, GA, USA

[3] School of Science, University of Waikato (Tauranga), Tauranga, New Zealand

[4]Geophysical Laboratory, Carnegie Institution for Science, Washington DC, USA

[5]School of Earth and Environment, University of Leeds, Leeds, UK

*Corresponding authors: Email: noah.planavsky@yale.edu

ABSTRACT

The carbonate carbon isotope record has been traditionally interpreted as evidence of stability in the globally integrated ratio of organic to total carbon burial from Earth's surface environments over the past ~3.8 billion years, but recent work has begun to question this conclusion. Herein, we use a reactive-transport modeling approach to track organic carbon oxidation at varying atmospheric oxygen levels and use that information to provide a rough estimate of net primary production through time. Our results support the emerging view that there was extensive variability in the fraction of carbon buried as organic matter ($f_{b,org}$) throughout Earth's history. We strengthen the case that the carbonate carbon isotope record has been characterized by a relatively constant baseline value over time due to a fundamental mechanistic link between atmospheric O_2 levels and the carbon isotope composition of net inputs to the ocean-atmosphere system. Further, using estimates of the organic carbon burial flux ($F_{b,org}$) and the burial efficiency of the carbon pump from our marine reactive-transport modeling, we also support previous work suggesting extensive fluctuation in marine net primary production over time.

Keywords: Carbon burial, marine NPP, reactive transport modeling, atmospheric oxygen level.

INTRODUCTION

The sedimentary carbon isotope record is one of the key tools used to reconstruct the evolution of the global carbon cycle (Schidlowski and others, 1976; Holland, 1984; Schidlowski, 1988; Kump and Arthur, 1999; Berner and others, 2003; Horwath, 2006; Hayes and Waldbauer, 2006). Further, because carbon weathering, degassing and burial play major roles in controlling atmospheric carbon dioxide and oxygen levels, carbon isotope data have been essential for developing a quantitative understanding of the evolution of Earth's atmospheric composition (for example Berner and others, 2003). Carbon is removed from the ocean-atmosphere system primarily through two burial fluxes in marine sediments—carbonate carbon and organic carbon. Carbonate carbon isotope values track dissolved inorganic carbon (DIC) values of the fluids from which they precipitate, and it is, therefore, in theory, possible to reconstruct the isotopic composition of seawater through time by measuring the C-isotope composition of marine carbonate rocks (fig. 1). In contrast, organic carbon is characterized by strongly negative $\delta^{13}C$ values ($\delta^{13}C = 1000 * [(^{13}C/^{12}C)_{sample}/(^{13}C/^{12}C)_{VPDB} - 1]$) as a result of large isotope fractionations during enzymatic carbon fixation into biomass. At steady state, marine $\delta^{13}C_{DIC}$ vales are conventionally interpreted to track the balance between organic and carbonate carbon burial fluxes on a global scale, conventionally expressed as the relative burial fraction of organic carbon ($f_{b,org}$) (Kump and Arthur, 1999):

$$f_{b,org} = \frac{input \quad b,carb}{B} = \frac{F_{b,org}}{F_{b,org}+F_{b,carb}} \quad (1) .$$

This framework has been widely applied to estimate the relative extent of organic carbon burial by using estimates of the isotopic difference between the burial fluxes of sedimentary organic matter (δ_{org}) and carbonate (δ_{carb}) ($\Delta_B = \delta_{org} - \delta_{carb}$), the isotope composition of aggregate inputs to the ocean (δ_{input}), and the carbon isotope composition of ambient seawater based on measurements of carbonate rocks (δ_{carb}). In theory, $f_{b,org}$ can also be reconstructed based on estimates of the flux of organic carbon burial, $F_{b,org}$, and flux of carbonate burial, $F_{b,carb}$.

For the vast majority of Earth's history Δ_B values have been between -32 and -25 per mil (‰) (Krissansen-Totton and others, 2015)—commonly interpreted as reflecting the enzymatic isotope effects during carbon fixation of Form I/II RuBisCO (ribulose-1,5-bisphosphate carboxylase/oxygenase) (for example Hayes, 2019). The integrated carbon input term δ_{input}, which includes carbon fluxes from carbonate and organic carbon weathering and metamorphic/volcanic

degassing, is typically assumed to have had a roughly constant value throughout Earth's history that mirrors the average $\delta^{13}C$ value of the mantle (~-5‰) (Stachel and others, 2009; Ickert and others, 2015; Howell and others, 2020). In this framework, consistent $\delta^{13}C_{carb}$ values near 0‰ (±1‰) through the entirety of Earth's history implies roughly constant $f_{b,org}$ values (Holland, 1984; Marais and others, 1992; Schidlowski, 2001) (fig. 1).

However, static $f_{b,org}$ values are enigmatic for a number of reasons. For example, under the assumption of a roughly similar carbon input flux to the ocean-atmosphere system over time, the carbon isotope record suggests that organic carbon burial rates have been largely invariant for the vast majority of Earth's history. This is a puzzling result, as there have been major secular changes to the organic carbon cycle like the rise of oxygenic photosynthesis, the proliferation of eukaryotic algae, and the expansion of land plants, among others. Constant $f_{b,org}$ values and invariant organic carbon burial fluxes are also difficult to reconcile with evidence for atmospheric oxygen levels over an order of magnitude below present atmospheric levels (PAL) throughout much of Earth's history (Canfield, 2005; Kump, 2008; Lyons and others, 2014). At low pO_2 levels, globally integrated oxygen consumption during weathering should be significantly reduced relative to the modern Earth (for example Laakso and Schrag, 2014; Derry, 2015), but this expectation is inconsistent with the notion of effectively modern organic carbon burial rates as deduced from the conventional application of carbon isotope mass balance (Holland, 1985; De Marais and others, 1992; Schidlowski, 2001).

Herein, we explore the idea that the extent of organic carbon oxidation in terrestrial weathering systems has changed dramatically through Earth's history, and that mechanistic links between organic carbon weathering and ambient atmospheric O_2 levels can parsimoniously resolve apparent paradoxes between the invariant carbonate carbon isotope record. Importantly, variations in the extent of organic carbon oxidation during weathering at Earth's surface would change the $\delta^{13}C$ value of the carbon input term—forcing a reinterpretation of the global carbon isotope mass balance. This idea has been outlined by previous works (Derry, 2015; Daines and others, 2017; Miyazaki and others, 2018). We add complexity to their calculations—and we show that some of the details we explore have important implications for the long-term carbon cycle. However, this work in essence supports, despite a more thorough exploration of the complexity of organic carbon oxidation, the simple calculations of Derry (2014) highlighting that changing organic carbon oxidation must have a major effect on how we interpret the long-term carbon isotope record. We build on this idea by demonstrating with most accepted scenarios for atmospheric oxygen evolution (for example Lyons et al., 2014), that changes in $F_{b,org}$ and atmospheric oxygen level lead to an extensive fluctuation in marine NPP. Therefore, our modeling exercise further supports multiple

recent suggestions for pronounced nutrient limitation (for example P) throughout most of the Earth's history (for example Laakso and Schrag, 2018).

We have constructed estimates of carbon isotopic and carbon flux variations over time that fit into the formulation of Kump and Arthur (1999). This requires assumptions about carbon isotopic values of various reservoirs, as well as the absolute fluxes between reservoirs. While most fluxes are assumed fixed, we vary the organic carbon weathering flux based on how quickly ancient organic matter is oxidized in soils. This oxidation rate depends on the assumed atmospheric oxygen level. This model calculates the penetration and consumption of oxygen in an eroding soil layer containing ancient organic matter in a boundary layer, converting the organic matter to CO_2 and H_2O. Some of the organic matter may be eroded off the top of the soil layer without complete oxidation (especially for high erosion rates and low oxygen levels). We also estimate oxidation that would occur while such organic matter is in the fluvial system (termed overbank oxidation), before ending up in the ocean where it may be buried. We use assumed probability density functions of erosion rate and organic carbon concentrations at depth to provide more robust estimates of the amount of organic matter being eroded for a given atmospheric oxygen level—allowing us to, at any time interval, provide a ne of organic carbon burial based on carbonate carbon isotope value and other standard assumptions.

We build from estimates of organic carbon burial to provide rough estimates on the extents of marine net primary productivity using a simple marine organic carbon burial model. The basic idea behind linking organic carbon burial and primary productivity is straightforward. However, atmospheric oxygen levels (and marine oxygen levels) would have strongly influenced how net primary production and organic carbon burial are linked. At steady state, the flux of organic carbon burial can be estimated as:

$$F_{b,org} = f_{b,org} * F_{\text{input}} \quad (2),$$

where $F_{b,org}$ is the flux of organic carbon burial and F_{input} is the sum of carbon fluxes from the crust and weathering of carbonates and organic matter. This flux relates to marine net primary production through the efficiency of the carbon pump:

$$F_{b,org} = \varepsilon * \text{NPP} \quad (3).$$

Here ε is the burial efficiency of the carbon pump and NPP is net primary production. It is likely that the values of both burial efficiency and NPP would have greatly fluctuated throughout Earth's history due to changes in atmospheric oxygen levels, which would have been tightly linked to changes in $F_{b,org}$ (for example Laakso and Schrag, 2014; Derry, 2014; 2015).

DESCRIPTION OF THE MODELS

Oxidation via weathering of organic matter and its dependence on atmospheric oxygen

Our biogeochemical reactive transport model is meant to mimic subaerial weathering in black shales at varying atmospheric oxygen levels (fig. 2) (Bolton and others, 2006). We model shale weathering given that most of the organic carbon at Earth's surface will be hosted in black shales, despite the fact that this rock type comprises only ~20% of the upper continental crust (Bluth and Kump, 1991). We use probability distributions for organic matter concentrations (see below) to help account for both low and high amounts in eroding landforms. Redox dynamics in the model are controlled by the kinetics of organic matter (OM) and pyrite oxidation driven by diffusion of atmospherically derived gaseous O_2, via

$$CH_2O + O_2 = CO_2 + H_2O \quad (4)$$

$$4\ FeS_2 + 15\ O_2 + 8\ H_2O = 2\ Fe_2O_3 + 8\ H_2SO_4 \quad (5)$$

where CH_2O represents a simplified stoichiometric formula for OM, and the reverse of the first equation represents OM burial. Oxygen diffusion occurs through interconnected pore spaces and gaseous O_2 incorporated into water films on sediment grains via Henry's law. As weathering proceeds, the grains of OM and pyrite reduce in size affecting their surface areas and the overall soil porosity. Given that pyrite and organic matter are by far the dominant reductants in black shales we have not included oxidation of non-sulfide bearing ferrous iron phases. We focus on organic carbon oxidation and provide only a limited exploration of sulfide oxidation. For most simulations we ran, except those at very high erosion rates (over 15 cm/kyr), pyrite was largely oxidized in the critical zone (even before continental transport) when > 1% PAL (present atmospheric level) (for example fig. 3). The amount of pyr_{top} decreased rapidly with increasing pO_2 and depended weakly on TOC_{init}. This is in slight contrast to other work on C-S oxidation modeling (Daines and others, 2017) that reported non-quantitative pyrite oxidation over a wide range of atmospheric oxygen levels (for example pO_2 > 10% PAL). However, (Daines and others, 2017) used higher mean pyrite concentrations. We use values that are consistent with empirical records for most shales in

Neoproterozoic and Paleozoic (Sperling and others, 2015). Our model derivation and parameter choices are detailed in the Appendix.

To explore the broader significance of this local weathering model we incorporated the model results into to a global carbon isotope mass balance that includes organic carbon oxidation during both soil formation and downstream transport. Within a single weathering system, the quantity of organic carbon oxidized during weathering will depend most strongly on (1) the initial amount of organic matter in un-weathered bedrock (TOC_{init}), (2) denudation rate, (3) a continental transport time, and (4) atmospheric oxygen level. To extrapolate the weathering model results to a global scale, we have assumed statistical distributions for both TOC_{init} and denudation rates based on empirical data (Holland, 1978; Raiswell and Berner, 1986), and have weighted the organic matter oxidation fluxes from numerous 1-D model runs to compute a global organic carbon oxidation flux for Earth's weathering surface as a function of atmospheric pO_2. By accounting for the fact that there will be non-quantitative oxidation with high TOC_{init} values and high denudation rates, even at modern pO_2 levels, this approach provides a much more accurate and robust global estimate of organic carbon oxidation than the assumption of a single mean TOC_{init} value and erosion rate. Lastly, using the outputs of these integrations, we estimate the extent of oxidation during transport from soils to sedimentary basins (for example transport and floodplain oxidation) utilizing a model with evolving particle surface area and oxygen-specific carbon oxidation rates coupled to assumed transport times (see below). The transport time following erosion from the soil is poorly constrained even in the modern and is thereby one of the largest sources of uncertainty in our model. The end result of the weathering model is a global carbon oxidation flux that can be combined with carbonate carbon and volcanogenic carbon fluxes to the ocean-atmosphere system to get an estimate of the isotopic composition (δ_{input}) and magnitude of the global carbon input term at varying atmospheric oxygen levels. We tied our new estimates of carbon fluxes to the ocean atmosphere system into a commonly utilized global carbon isotope mass balance (Kump and Arthur, 1999). Our mass balance model relies on previously proposed fluxes for the global carbon cycle (Kump and Arthur, 1999), but allows for the isotope composition and magnitude of integrated carbon input term (δ_{input}) to vary with atmospheric oxygen levels. It is worth noting that long-term mass balance is maintained by assuming that organic carbon that was not oxidized will either be stored in the curst or subducted into the mantle.

Our weathering model is based on Bolton and others (2006), which has been shown to accurately reconstruct modern black shale profiles (Bolton and others, 2006). The model is based on kinetic controls of sedimentary organic matter and pyrite oxidation reactions. The downward diffusion of gaseous O_2 through the interconnected pore spaces partitions with dissolved O_2 in water

films on sediment grains via Henry's law. The model is time dependent, but the system reaches a steady-state given the presence of a denudation term, where the supply of unoxidized material is balanced with diffusion of oxygen and reaction in the soil profile. Pyrite reacts faster with O_2 than does organic matter (for a given local concentration of oxygen) making the pyrite front generally deeper and sharper than the organic matter front. The model resolves the boundary layer in the soil where these processes occur (typically using 400 grid points across the boundary layer) and is much more accurate than box models (for example Lasaga and Ohmoto, 2002) that do not resolve the boundary layer.

Our model is not designed for extremely wet or extremely dry environments. Arid environments may lack the water film that seems to be necessary for organic matter (OM) oxidation to occur and we do not include photochemical degradation. The model domain is assumed to be above the water table, which results in the model not being well suited to track areas with extreme rainfall. However, below the water table oxygen levels would generally be very low if OM were present. A detailed introduction to the conceptual and numerical model is presented in the Appendix.

Reconstructing marine NPP through time

In order to explore the effect of changes in the burial flux of organic matter ($F_{b,org}$) and atmospheric oxygen levels on marine net primary production, we built a one-dimensional steady-state reactive-transport model for the marine environment (described below). Our model is aimed at estimating the burial efficiency of the carbon pump at different atmospheric oxygen levels. The calculated burial efficiency, along with the revised $F_{b,org}$, is used to reconstruct the marine NPP through time (NPP = $F_{b,org}$ / ε; equation 3).

In order to provide an estimate for burial efficiency during the Archean, GOE, Proterozoic, and Phanerozoic, we use the following model to simulate the cycling of oxygen and iron in the water column. At steady-state:

$$0 = \frac{d}{dz}\left[K_z \frac{d\,C}{dz} - C(z)v(z)\right] \pm R \qquad (6)$$

Here z is depth below the photic zone, C is the concentration of the compound of interest, K_z is the turbulent diffusion coefficient, $v(z)$ is the advection velocity, and R represents the rate(s) of reaction(s) that consume or produce a given species. Values for the turbulent diffusion coefficient,

K_z, were assumed to be relatively high in the upper ocean above the chemocline to reflect the highly convective Ekman layer, linearly decrease in the thermocline to reflect the high impediment to vertical mixing caused by strong temperature stratification, and then linearly increase in the deep ocean where the absence of a strong temperature gradient permits more effective vertical mixing. The advection coefficient, *v(z),* was estimated by dividing the high latitude to deep exchange flux (~50 Sv; 1 Sv = 10^6 m^3/s) by the lateral (cross-sectional) area of the deep ocean. Due to the uncertainty involved with these estimations, the advection term was multiplied by a fitting parameter, α. Values for the turbulent diffusion coefficient at the surface, thermocline, and deep oceans along with the fitting parameter, α, for advection term were obtained by calculating a rough fit against the measured DIC and oxygen depth profiles of the modern oceans (fig. A1).

The rate of iron oxidation was assumed to follow first order kinetics:

$$R_{Fe} = k_{fe} [O_2] [Fe^{2+}] \quad (7)$$

For simplicity, the concentration of Fe^{2+} (in μM) was set to zero in the oxic zone and increases below the oxygen penetration depth (OPD) as:

$$[Fe^{2+}] = [Fe]_1 \sqrt{z - OPD} \quad (8)$$

where depth $z > OPD$ is in meters and $[Fe]_1$ is a constant. This mimics typical Fe^{2+} profiles in the sub-oxic zones of the modern freshwater and marine sediments and stratified water columns. The OPD is defined as the depth where the seawater oxygen level becomes less than 0.5 μM.

For oxygen, the consumption rates include the rates of aerobic respiration and iron oxidation in the anoxic water column. The rate of oxygen consumption by aerobic respiration was simulated using the Michaelis-Menten kinetics:

$$R_{resp} = R_C \frac{[O_2]}{K_i + [O_2]} \quad . \quad (9)$$

Here, constant K_i is the half-saturation constant (in the unit of μM) that, strictly speaking describes the affinity of enzymes for substrate, but that is commonly used to described microbial processes controlled by a suite of enzymes. R_C is the carbon mineralization rate, approximated as $R_C = k\,[OC]$ where the reactivity k was described by the Middelburg power law as a function of carbon age t *(year):* $\log_{10} k = -0.95 * \log_{10} t - 0.81$ (Middelburg, 1989). To account for the effect of enhanced organic matter degradation under oxic conditions, we used an updated version of the power law that distinguishes between the rate of carbon degradation under oxic versus anoxic conditions

(Katsev and Crowe, 2015). This power-law has been found to hold over a wide range of organic matter degradation timescales, ranging from fresh phytoplankton to sedimentary organic matter buried millions of years ago (Katsev and Crowe, 2015). The age (day) in the model is calculated using the settling rate of oceanic particles:

$$t_{age} = \frac{z_i}{u_{i,average}}, \quad (10)$$

where z_i is a given depth (m) and $u_{i,average}$ is the average velocity of aggregates at depth i (m/day). We also accounted for the effect of change in sinking rate of oceanic aggregates on the burial efficiency of the carbon pump. Generally, the eukaryote-dominated biological pump which emerged in the Neoproterozoic era is suggested to have promoted faster sinking fluxes of organic carbon through an increase in average cell size, greater propensity of eukaryotic algae to form particulate aggregates, and ballasting due to tests and scales (Lenton and others, 2014). This proposal implies that, prior to the ecological dominance of algae, sinking rate of oceanic aggregates in a cyanobacteria-dominated biological pump would have been slower. However, given that aggregation will occur regardless of cell size (for example Laurenceau‐Cornec and others, 2019) we show results with both a slower and a near modern sinking rate of aggregates for the Precambrian (Fakhraee and others, 2020; Fakhraee and others, 2021). Finally, burial efficiency is calculated as the ratio of the organic carbon amount at the top of our domain to the amount that was buried in the deep sediment.

Depending on the value of burial efficiency of organic carbon in the water column, a fraction of organic matter delivered from the water column would also be degraded in the sediment during early diagenesis. The burial efficiency used to calculate the marine net primary production would then be as the fraction of organic matter reaches the seafloor multiplied by the burial efficiency of organic matter in the sediment. To account for the effect of oxygen in facilitating the organic matter degradation, thereby decrease the burial efficiency, we used the previously published dataset for the range of burial efficiencies in modern oxic and anoxic sediments (Table A5; Katsev and Crowe, 2015). Finally, to consider the impact of the uncertainty involved in choosing modeling input parameters, we employed a stochastic approach, in which variables were randomly sampled within the expected range (Table. A5) allowing us to obtain the most probable values for burial efficiency over geological time.

MODELING RESULTS

Results of the biogeochemical weathering model

We first calculated how much ancient OM would be oxidized and expected to survive during erosive processes at the Earth's surface for various atmospheric oxygen levels. Those results also depend upon how much ancient OM is exposed to erosion and upon the erosion rates. This naturally leads to running the model for ancient OM oxidation of Bolton and others (2006) for a 'computational cube' involving oxygen levels, erosion rates, and OM content exposed at the eroding surface. To estimate the global flux of unoxidized OM to the ocean, we draw from probability distributions that represent spatial distributions of erosion rate and ancient OM at depth. Additional OM oxidation during fluvial transport to the oceans in transitory overbank deposits. Once a collection of fluxes of oxidized OM has been computed, we then apply the formulation of Kump and Arthur (1999) to estimate global carbon fluxes at a given carbonate carbon isotope value.

The model of Bolton and others (2006) was run to a steady state with typically 400 grid points spanning the boundary layer (cf. fig. 3), except for cases clearly leaving no OM at the surface. TOC (total organic carbon) at depth (TOC_{init}) was set at 0.1, 0.5, 0.75, 1, 2, 3, or 5% (mass % of C in dry mass) and the pyrite concentrations at depth were set at 0.2 or 0.4% (mass% of dry mass: pyr_{init}). The pO_2 values were set at 0.1, 1, 4, 10, 15, or 18% PAL (percent of the present atmospheric O_2 concentration). Erosion rates (*er*) were set to 1.19, 2.5, 5, 7.5, 10, 15, 20, 30, 40, 50, 250, or 500 cm/kyr. Other parameter values are listed in tables in the Appendix. The results were used to set up a matrix (with index order %PAL, TOC_{init}, *er*) of the extent of carbon oxidation that was used for contour plots and probability distributions functions used for the global carbon isotope mass balance modeling. For all of the simulations we ran, except those at very high erosion rates (over 30 cm/kyr) pyrite was essentially completely oxidized at the surface for pO_2=18%. PAL. The amount of pyr_{top} decreased rapidly with pO_2 and depended only weakly on TOC_{init}.

Sensitivity results for OM and pyrite oxidation for various pO_2 varying kinetic rates

We have explored the sensitivity of our results to varying oxidation rate laws, given that there are uncertainties in both OM and pyrite oxidation rate laws (fig. 4), where rates were taken as 0.1, 0.5, 1, 2, or 10 times the default rates for OM oxidation and 0.5, 1, 2 times the default oxidation rate for pyrite. pO_2 was varied as described above, but the erosion rate was fixed at 5 cm/kyr, the TOC and pyrite at depth (TOC_{init}, pyr_{init}) were set at 0.75% and 0.4%, respectively. The

rates of the oxidation reactions vary with the local oxygen concentration at depth in the reaction zone. Figure 4 shows the variation of TOC remaining at the surface for various OM kinetic rate multipliers as a function of pO_2, with less TOC remaining at the surface when the rate is larger. For the lowest pO_2 (0.1%PAL) case, TOC_{top} is very near to the 0.75% value set at depth. Given the dearth of experimental studies on kerogen oxidation it is difficult to gauge how to translate uncertainties in rate law choices to error in the globally integrated extents of organic carbon oxidation. However, given that it is possible to model modern organic weathering profiles with existing rate laws (for example (Bolton and others, 2006) we, tentatively, suggest it likely that the potential error associated with rate law choices is much less than that associated with estimates of average and distribution of erosion rates and estimates of the extent and distribution of organic carbon in the upper continental crust.

For contour plots we used interpolation schemes in order to develop contours on an appropriately sized grid. We interpolated TOC_{top} and an organic oxidation term (herein *used* = TOC_{init} -TOC_{top}) as a function of pO_2, TOC_{init} and *er* (the erosion or denudation rate) (on a grid of 100x99x100, respectively, the indices of which are often taken as *i, j, k* below). We used the R function splinefun with the "monoH.FC" method to avoid overshoots (producing a monotone hermite spline using the method of (Fritsch and Carlson, 1980). We also ignored values of TOC_{top} equal to zero in the interpolation scheme and set interpolated values to zero if they were negative. We first interpolated from the coarse grid in *er* to a fine grid, then used the resulting arrays to interpolate the grid in TOC_{init} to a fine grid, followed by interpolation of pO_2 from a coarse to fine grid (the order was important). The results of TOC_{top} contoured vs. pO_2 and TOC_{init} for various erosion rates are shown in figure 5 for pyr_{init} = 0.4%. For the lowest erosion rate (1.19 cm/kyr), essentially all of the OM is oxidized when the oxygen levels reach ~10 (%PAL). More rapid erosion rates and higher TOC_{init} allow more OM to be left at the surface without oxidation as would be expected and as is observed in modern settings. In figure S1 (online supplement) we show pyr_{top} contoured vs. pO_2 and TOC_{init} for various erosion rates and for pyr_{init}=0.4%. For expected mean erosion rates (for example 5 cm/kyr) surface pyrite concentrations are minor (<0.1%) when pO_2 is above 1% PAL. Figure 6 displays essentially the same information as figure 5, but for *'used'* = (TOC_{init} -TOC_{top}). This variable (*used*) is used below in the global carbon isotope mass balance calculations.

Mix of TOC_{init} using distribution functions

On a global scale eroding sediment contains variable initial amounts of TOC at depth (TOC_{init}). To include the influence of TOC_{init} heterogeneities for–different locations, we can

calculate the expected values of TOC_{jnit} sampled from probability distributions. From these distributions, we can also calculate expected values of quantities like TOC_{top} and the extent that TOC is oxidized. We estimated globally representative TOC_{init} values from a series of beta distributions. More specifically, one flavor of a beta distribution over a finite interval from L to U (applied to the lower and upper limits of the TOC_{init} modeled) is adapted from AbouRizk and others (1994) to create a discrete probability density function (PDF) using $x_j = TOC_{init:j}$ with j=1 to n

$$f(x_j) = \left(\frac{1}{N}\right)\left((x_j - L)^A (U - x_j)^B\right) \quad (11)$$

(using $A=a-1$ and $B=b-1$ for comparable notation), where N is a normalization factor. N can be computed from Gamma functions and the interval $dx=x_j-x_{j-1}$ but we did the normalization numerically to assure that $\sum_j f(x_j)=1$. We used A=1, L=0.1%, U=5%, and $dx=(U-L)/(n-1)$ =0.05 with n=99 equally spaced values of x. We also used a series of B values with B_{max}=40, B_{min}=2, $m=(B_{max} - B_{min})/(n-1)$, and $B=m(i-1)+B_{min}$, for i=99 down to 1, to yield the expected value of TOC_{init} = 0.3313 for B_{max} and the expected value for TOC_{init} = 2.060 for B_{min}. We display 11 of the 99 PDFs in figure A2 (appendix) along with how the expected value (mean) of TOC_{init} and the standard deviation of the distributions depend on B. (One can relate the discrete distribution values of f_j to a continuous distribution $f_{c:i}$ by $f_j=f_{c:j}*dx$). We also call these distributions $f(OM)$.

Writing $u(j)$ for $'used_j'$ = ($TOC_{init:j}$ -$TOC_{top:j}$) for the jth index of x_j= $TOC_{init:j}$, the expected value of u for the jth beta distributions $f_j(x_J)$, can be calculated using $\langle u \rangle_j = \sum_J f_j(x_J)u(J)$. (Here, J refers to the TOC_{init} index, and j refers to which beta distribution is chosen). These expected values are calculated for each pO_2 and are thus functions of the expected values of TOC_{init} as found above. These expected values of *used* are displayed in figure A3 and are used in the calculations of carbon isotopic burial values and fluxes as described below.

A mix of erosion rates

On a global scale, erosion rates will also be variable. To incorporate this into our estimates of the extent of globally integrated extents of organic carbon oxidation during weathering at varying pO_2 levels we not only consider variable amounts of initial organic carbon present in rocks being weathered (from the probability density functions), but also variable erosion rates. This is also done using representative probability distributions. Current erosion rates are not known with great accuracy, but we have estimated that from probability distributions derived from (Larsen and others, 2014b). To cover a wider range of possible erosion rates, we also modified the distribution rooted in Larsen and others and made use of modified beta distributions in a way similar to those

used for the distributions of TOC_{init} above (Larsen and others, 2014b; see also Dixon and von Blanckenburg). To the beta distributions, we added linear functions with small but finite probabilities at the lowest erosion rate considered (1.1900 cm/kyr with *f(er)* between 0.0029 and 0.0090 based on a 100-point distribution) and erosion rates (*er*) of 50 cm/kyr (with *f(er)* between 3.7×10^{-6} and 6.9×10^{-4}). Between 50 and 500 cm/kyr rates, we added functions of similar form to the Larsen-derived distribution. All erosion rate pdfs used had 100 bins, equally spaced in $\log_{10}(er)$ space. Figure A4 shows these probability distributions.

We note that Daines and others (2017), used distributions calculated from Milliman and Meade (1983), but these have the serious disadvantage that those erosion rates are basin-wide averages for each river included in that dataset. Given that we aim to calculate the effect of OM oxidation in a boundary layer at a local scale and use this for global estimates, high-resolution estimates of erosion rate would be desirable. We note that our use of the term 'erosion rates' is equivalent to total denudation rates, being the sum of physical and chemical weathering. If there were no uplift, and in quasi-steady-state, the un-weathered bedrock below the chemical weathering zone would move downward at the same rate as the land surface. In the zone above the bedrock, there are tendencies to increase the porosity by chemical weathering and to decrease the porosity by compaction. Assuming a quasi-steady-state with the uplift rate equal to denudation rate, the land surface and the bedrock surface would remain stationary.

The 'Larsen-derived' denudation rates were calculated based on the global-scale mean local slope in Larsen and others (2014b) (Larsen and others, 2014b). In Larsen and others (2014b), slope data was calculated using a 3 arc-second (~90 m at the equator) digital elevation model (DEM) with worldwide coverage (www.viewfinderpanoramas.org). Accurate slope angles were obtained by calibrating the pole-ward convergence of meridians. Afterwards, mean local slope for each grid point was determined by centering a 5×5 km square box on that grid point and averaging all the slopes (at the ~90 m scale) located within the square box. The original data set (mean local slope) from Larsen and others (2014b) is located at: http://gis.ess.washington.edu/grg/publications/support/. The geographic coordinate system is GCS-WGS-1984. To account for the latitudinal variation in grid cell area, the original data set was projected into World Cylindrical Equal Area using ArcMap 10.4.1. In this way, the mean local slope is now normalized to the area of Earth's surface. Based on the new set of mean local slope data, Larsen and others (2014b) used a denudation rate (D, cm/kyr) following the nonlinear equation derived from Willenbring and others (2013) (Willenbring and others, 2013), $D = 1.19e^{6.5\times\tan\theta}$, where $\tan\theta$ is the mean local slope (m/m). Following the procedure of Larsen and

447 others (2014b), we imposed a maximum denudation rate of 1000 cm/kyr, which is close to the most
448 rapid denudation rate that have been measured using ^{10}Be (Larsen and others, 2014a).
449
450 To create the probability density function (pdf) of the global-scale denudate rate, we
451 created 500 equally-spaced bins from 0 to 1000 cm/kyr. All the denudation rates were grouped
452 into these 500 bins and the number of denudations in each bin was calculated, from which the pdf
453 could be obtained. Erosion rates higher than 1000 cm/kyr were lumped into the 1000 cm/kyr bin.
454 From the pdf using 500 bins, we projected this onto a pdf of 100 bins, equally spaced in $\log_{10}(er)$
455 space between 1.19 and 500 cm/kyr and lumped the erosion rates higher than 500 cm/kyr into that
456 bin, as further discussed in the caption of figure A4. The discrete probability density functions were
457 all renormalized, so they sum to unity. Averages of 500 and 100 bin versions differ slightly (the
458 mean of the 100-point version in log10 space is 3.43, while that of the 500 point version is 3.57).
459
460 In figures S4 and S5 we use the distributions with respect to both TOC_{init} and *er* as
461 presented above to calculate the expected values of TOC_{top} ($< TOC_{top} >$) and *used*, respectively, for
462 two selected values of the mean denudation rates. The relevant formula for $< TOC_{top} >$ is similar
463 to the $<u>_j$ expression above using TOC_{top} instead of *'used'*.
464
465 **Overbank Oxidation**
466
467 Carbon oxidation will also take place during transport to the marine realm (for example
468 overbank oxidation). We have done calculations to estimate this effect, which can decrease the
469 amount of unoxidized OM delivered to the ocean. To incorporate this process into the global
470 isotope mass balance we have included an overbank oxidation term that is dependent on pO_2 levels
471 and on the extent of carbon delivered by erosion of unoxidized OM from the initial site of carbon
472 oxidation and delivered to the fluvial system. We use the same kinetics for OM oxidation as
473 described above. From figure 2 of Bolton and others (2006), (based on Chang and Berner, 1999),
474 the rate of OM oxidation (in moles C oxidized /(m^2 s)) at pO_2=1 PAL is 2.65×10^{-12}, or
475 (R_{yr}=8.3575×10^{-5} mol C/(m^2 yr)*(pO_2 (%PAL)/100)$^{0.30809}$) for general pO_2 using the power law
476 form for the kinetics (the exponent value was inadvertently omitted from the original publication).
477 This form includes the Henry's Law partitioning discussed above, so can be calculated directly
478 from the atmospheric O_2 levels. As was assumed in Bolton and others (2006), the shape of the OM
479 particles is assumed to retain its aspect ratio during oxidation, with the widths α times the thickness
480 *d*, so that the evolving surface area and particle volume are $2\alpha(2+\alpha)d^2$ and $\alpha^2 d^3$, respectively,
481 during the changes in particle thickness *d* (implying that the edges oxidize slightly faster than the

thickness to preserve shape during oxidation). We used α =5 and d_{init}=10^{-5}m. By the time the particle reaches the surface due to erosion, the particle size is d_{top}= d_{init}(TOC$_{top}$/TOC$_{init}$). Using eq. A9,

$$g_{OM:init}\left[\frac{\text{mole C in OM}}{\text{cm}^3\ \text{bulk}}\right]=\left(\frac{\left(TOC\%_{init}/100\right)\times\left(\rho_{solid}=2.5\text{g/cm}^3\right)}{MW_i\left[\frac{12.01\text{g C}}{\text{mole C}}\right]\cdot\left(\frac{1}{\left(\rho_{B,solid}=0.95\right)}\left[\frac{\text{cm}^3\ \text{bulk}}{\text{cm}^3\ \text{solid}}\right]\right)}\right)=1.978\times10^{-3}\cdot TOC\%_{init} \quad (12)$$

then using eq. A10, the volume fraction of OM is

$$\phi_{OM,solid}\left[\frac{\text{cm}^3\ \text{OM}}{\text{cm}^3\ \text{bulk}}\right]=\left(\frac{g_{OM:init}\left[\frac{\text{mole C in OM}}{\text{cm}^3\ \text{bulk}}\right]\cdot\left[\frac{15.171\text{ g OM}}{\text{mole OM}}\right]}{\left(\rho_{OM}=2.26\right)\left[\frac{\text{g OM}}{\text{cm}^3\ \text{OM}}\right]\cdot\left(\frac{1\text{ mole C in OM}}{1\text{ mole OM}}\right)}\right)=6.713\cdot g_{OM:init} \quad (13)$$

Note that the above quantity has the same numeric values in m^3/m^3.

We then use $\bar{N}_{OM}$= $\phi_{OM,solid}/(\alpha_{OM}{}^2\, d^3{}_{OM:init})$, with units of number per m^3 to calculate the number of OM particles per m^3 as 5.310x10^{11}*TOC$_{init}$(%). As long as the particles have finite size, this "nucleation density" remains constant during oxidation. The molar volume of C in OM (in m^3/mol) is $\bar{V}_C$ =(15.171(g OM/mol C)) / (2.26x10^6 (g/m^3)) =6.713x10^{-6}. Then we calculate the number of mol C per particle of OM peeling off the top of the eroding surface as the volume per particle divided by the molar volume to yield h_o =$\alpha^2 d^3{}_{top}$ /$\bar{V}_C$ =$\alpha^2 d^3{}_{init}$ /$\bar{V}_C$ = 3.724x10^{-9}(TOC$_{top}$/TOC$_{init}$). The rate of change of the mol C per particle once it is injected into the fluvial system is proportional to its evolving surface area and the assumed kinetics, as the water should be well mixed and in Henry's law equilibrium with the atmosphere, as:

$$\frac{\partial h}{\partial t}=-2\alpha(2+\alpha)d^2R_{yr}(pO_2(\%PAL)/100)^{0.30809} \quad (14)$$

But d=$(h\bar{V}_C/\alpha^2)^{1/3}$ so that h evolves as

$$\frac{\partial h}{\partial t}=-2.432\times10^{-7}\,h^{2/3}(pO_2(\%PAL)/100)^{0.30809} \quad (15)$$

Writing a=2.432x10^{-7} with B=a*$f(O)$ =2.432x10^{-7}*(pO_2 (%PAL)/100)$^{0.30809}$ the equation dh/dt=–B*$h^{2/3}$ has the solution

$$h=((-B*t_{OB}(\text{years})+3h_o{}^{1/3})/3)^3 \quad (16)$$

for t_{OB} years of exposure to secondary oxidation (we force h to be non-negative). The amount of mol C oxidized per particle in the fluvial system is then h_o-$h(t)$. The particles eroded per kyr is a

product of the land surface area (1.48×10^{14} m^2), the erosion rate, and the particle nucleation density (with appropriate unit adjustments), or er(cm/kyr) * SA_{land} * $\bar{N}_{OM}$ * (1 m/100cm). This implies that the overbank oxidation (F_{OB} in 10^{12} mol C/kyr) is $(h_o\text{-}((-B*t_{OB}(\text{years})+3h_o^{1/3})/3)^3)* er * 1.48\text{x}10^{14} *5.310\text{x}10^{11}*(TOC_{init}\%/100)*10^{-12}$, or the probability distributions may be used. Using the probability density functions with respect to the erosion rate, *f(er)*, and with respect to the distribution of TOC_{init}, *f(OM)*, to form an estimate of the oxidation of C (in 10^{12} mol C/kyr),

$$F_{OBi,j,k} = \sum_K \sum_J f(er)_{k,K} f(OM)_{j,J} (7.859\times10^{11}) er_K TOC_{init:J} \left\{ (3.724\times10^{-9}) \left(\frac{TOC_{top}}{TOC_{init}} \right)_{i,J,K} - \frac{1}{27} \left[3 \left[(3.724\times10^{-9}) \left(\frac{TOC_{top}}{TOC_{init}} \right)_{i,J,K} \right]^{1/3} - (2.432\times10^{-7}) t_{OB} \left(\frac{pO_2(\%PAL)}{100} \right)_i^{0.30809} \right]^3 \right\} \quad (17)$$

where the indices, i, j, k, refer to the interpolated fits with respect to $pO_{2:i}$, $TOC_{init:j}$, and the erosion rate variable er_k. We explore the influence of overbank oxidation on the burial flux of organic carbon by adding $F_{OB,org}$ to $F_{w,org}$ (see below). Transport time in continental settings has been estimated to be between less than 10 kyr to about 400 kyr (DePaolo and others, 2012) using U-series comminution techniques. Here we consider the transport times in which oxidation was occurring of 1000 years and 10,000 years to illustrate the importance of this process.

Calculation of carbon fluxes and carbon isotope mass balance

We now use the results of the modeling described above to estimate carbon fluxes and carbon isotopic values using Kump and Arthur (1999) framework. We have adopted similar notation to describe the global carbon isotope mass balance as that used by Kump and Arthur (1999) as well as a 'standard' carbon isotope mass balance (Kump and Arthur, 1999; Wallmann and Aloisi, 2012). Our preferred carbon isotope values for each flux and the magnitude of fixed fluxes are presented in Table A4. The obvious contrast with previous work is that we are varying the magnitude of the organic matter weathering flux that we define as:

$$F_{w,org} = 2927*er(\text{cm/kyr}) *< (TOC_{init} - TOC_{top})> \quad (18)$$

for a fixed erosion rate (in units of 10^{12} mol C/kyr). If overbank oxidation is included in $F_{w,org}$, the flux from eq. 17 must be added to the $F_{w,org}$ expressed in eq. 18. The factor 2927 comes from unit

conversions involving the porosity, bulk soil density, OM density, molecular wt. of C, and the current land surface area of 1.48 x 10^{14} m^2. For $F_{w,org}$ to have units of 10^{12} mol C/kyr, with *er* in cm/kyr, TOC in mass%, the factor (2927) carries units of 10^{12} mol C/(cm*mass fraction in %), and is explicitly calculated from the atomic mass of C, the average solid density, the volume fraction of solid in the bulk, unit conversions, and the (current) surface area of the Earth as:

$$\frac{1\ \text{mol C}}{12.01\ \text{g C}} \times \frac{2.5\ \text{g solid}}{\text{cm}^3\ \text{solid}} \times \frac{0.95\ \text{cm}^3\ \text{solid}}{\text{cm}^3\ \text{bulk}} \times \frac{10^6\ \text{cm}^3\ \text{bulk}}{\text{m}^3\ \text{bulk}} \times \frac{1\ \text{m}}{100\ \text{cm}} \times \frac{\text{fraction}}{100\%} \times 1.48\ \ 10^{14}\ \text{m}^2 \times 10^{-12}$$

If the erosion rate is drawn from a prothe bability density function (pdf), we sum over the pdf with respect to the erosion rate. For the erosion rate index *k*, and with *'used'* taken from the probability distribution with respect to TOC_{init}, the weathering flux is written out explicitly as (using the same i,jthe ,k indices referred to above):

$$\left(F_{w,org}\right)_{i,j,k} = \sum_{J}^{99} \sum_{K}^{100} 2927 er_K f(er)_{k,K} f(OM)_{j,J} \left(\text{TOC}_{init} - TOC_{top}\right)_{i,J,K} \qquad (19)$$

We can also calculate the delivery of OM to the fluvial system (with the same units of 10^{12} mol C/kyr) using the probability density functions as:

$$(F_{DF})_{i,j,k} = \sum_{J}^{99} \sum_{K}^{100} 2927 er_K f(er)_{k,K} f(OM)_{j,J} TOC_{top:i,J,K} \qquad (20)$$

We show how $F_{w,org}$ and F_{DF} depend on the parameter space in figures S6 and S7, respectively.

The influence of overbank oxidation on the weathering flux of organic carbon is estimated by adding $F_{OB,org}$ to $F_{w,org}$. The overbank oxidation flux is illustrated in figures S8 and S9. This directly translates into highly variable integrated carbon input isotope values (δ_w') at varying atmospheric oxygen levels (Fig. 6). It is worth noting that F_{DF} is a flux of unoxidized OM. The portion of that which is not oxidized during transport and time in overbank settings is simply reburied and is in a sense 'hidden' from the ocean/atmosphere carbon cycle.

Following Kump and Arthur (1999), we assumed a reservoir size, M_{oa} for carbon in the ocean-atmosphere system as 3.9x10^{18} mol C. The change in mass of C in the ocean-atmosphere system with time can be defined as:

$$(dM_{oa}/dt) = F_{volc} + F_{w,org} + F_{w,carb} - F_{b,org} - F_{b,carb} \quad (21)$$

We also define

$$F_w' = F_{volc} + F_{w,org} + F_{w,carb} \quad (22)$$

where we ignore the silicate weathering contribution to the total ocean-atmosphere system for C, because CO_2 drawdown during weathering is transported to the ocean as dissolved C species thus not changing the C in the total system (for example Kump and Arthur, 1999). The change with time of the product of the oceanic carbon isotopic values (δ_o) and the mass of the ocean-atmosphere system is assumed to be:

$$(d(\delta_o M_{oa})/dt) = F_{volc}\delta_{volc} + F_{w,org}\delta_{w,org} + F_{w,carb}\delta_{w,carb} - F_{b,org}\delta_{b,org} - F_{b,carb}\delta_{b,carb} \quad (23)$$

which may be rewritten as:

$$(d(\delta_o M_{oa})/dt) = M_{oa}(d\delta_{o,carb}/dt) + \delta_o (dM_{oa}/dt) \quad (24)$$

If we now assume steady state, the input fluxes to the ocean atmosphere system balance the burial fluxes, so defining δ_w' (δ_{input} in Eq. 1) through:

$$\delta_w' = (F_{volc}\delta_{volc} + F_{w,org}\delta_{w,org} + F_{w,carb}\delta_{w,carb})/ F_w' \quad (25)$$

and assuming $d\delta_{o,carb}/dt$ vanishes at steady state, and using the definition of Δ_b ($=\delta_{b,org} - \delta_{b,carb}$), and assuming all the carbonate isotopic signatures are identical to the oceanic values (δ_o), we have at steady state:

$$f_{b,org} = \frac{F_{b,org}}{F_w'} = \frac{\delta_w' - \delta_{carb}}{\Delta_b} = \frac{F_{b,org}}{F_{b,org} + F_{b,carb}} \quad (26)$$

For theoretical steady-state Earth system with a marine DIC value of 0‰ ($\delta_{b,carb} \approx 0$‰) we use a Δ_b of -30‰. The dependence of δ_w' and $f_{b,org}$ on the expected value of TOC_{init} from the beta distributions and pO_2 are shown for several specific modeled erosion rates in figures 7 and 8, respectively. Note that δ_w' becomes more negative with increasing pO_2 and increasing average

600 TOC_{init}, but the trends with increasing erosion rate are subtler. On the other hand, $f_{b,org}$ shows the
601 opposite trends with respect to pO_2 and TOC_{init}.
602
603 Figures S10 and S11 show, respectively, how δ_w' and $f_{b,org}$ depend on the expected values
604 of TOC_{init} and er, as well as pO_2 and overbank oxidation times. Figures 9-11 show the dependence
605 of $F_{b,org}$, $F_{b,carb}$, and $f_{b,org}$, respectively, on pO_2 for several overbank oxidation times and mean
606 erosion rates.
607
608 To more directly link our modeling approach to global carbon cycle records we provide
609 estimates of the variations in $f_{b,org}$ throughout Earth's history building from steady-state expressions
610 of the carbon cycle. We start our analysis at 3.5 Ga when there is clear empirical evidence for the
611 presence of carbonates with carbon isotope values near 0 ‰ (Krissansen-Totton and others, 2015),
612 and note that establishing a crustal carbonate reservoir with a near modern carbon isotope
613 composition likely involved more organic carbon burial on the early Earth than our model predicts
614 for the later Archean (see below). Although we are focusing on changes through time, we can use
615 the carbon isotope record to provide an archive of successive steady states (given that the carbon
616 cycle will be in steady state on a sub million-year time scale). The modeling above (eq. 19) provides
617 estimates of $F_{w,org}$ (which can include overbank oxidation effects as noted above) for various
618 erosion rates, oxygen levels and TOC_{init}. We can also vary $F_{w,carb}$, the land surface area, et cetera.
619 We estimate δ_w' (δ_{input}) values with varying oxygen levels using eq. 25 and estimate F_w' using eq.
620 22. We depart from some of the assumed default values in the tables in the Appendix, by using
621 smoothed (LOWESS filtered) observations of $\delta_{b,carb}$ and $\delta_{b,org}$ from Krissansen-Totton and others
622 (2015) from which Δ_b can be calculated (note that our Δ_b is their -ε). We then use

623 $$f_{b,org} = \frac{\delta_w^{'} - \delta_{b,carb:record}}{\Delta_{b:record}} \quad (27)$$

624
625 and

626 $$F_{b,org} = f_{b,org} \times F_w^{'} \quad (28)$$

627 to calculate these quantities using the sediment isotope records ('record').
628
629 We divided estimates of atmospheric pO_2 into three age bins, each with an upper and lower
630 oxygen level assumed to bound estimates of $f_{b,org}$ and $F_{b,org}$. For the Archean (4000Ma to 2500 Ma)
631 we used pO_2 = 0.1% PAL as an upper limit and assumed no oxidation for the lower oxygen limit
632 (making $F_{w,org}$=0) (Crowe and others, 2013; Lyons and others, 2014). For the early to middle
633 Proterozoic (2500Ma to 800 Ma) we used 5% PAL (solid lines) for the upper limit, and pO_2 = 0.5%

PAL (dashed lines) for the lower limit (for example Lyons and others, 2014; Planavsky and others, 2018). For the late Proterozoic and Phanerozoic (800 Ma to present) for the upper limit we assumed all OM was oxidized, and for the lower limit we used pO_2 = 18% PAL (for example Och and Shields-Zhou, 2012; Lyons and others, 2014). We note, however, there late Proterozoic and Paleozoic atmospheric oxygen levels are still poorly constrained. The expected value of TOC_{init} was fixed at a mean value of 0.75%. We also consider different terrestrial transport (overbank oxidation) times—0, 1kyr and 10 kyr. Figure 12 shows the values of Δ_B and $\delta_{b,carb}$ obtained from the smoothed observation. Figures 13 and 14 show the relative and absolute OM burial fluxes from Eqs. 27 and 28 for a wide range of conditions (see caption for Fig. 14).

The stability of the carbonate carbon isotope record throughout Earth's history is due to oxygen release from organic carbon burial driving a shift in the carbon isotope value of the input term to more ^{12}C-enriched values. As a result, the carbonate carbon isotope record does not provide a signal for constant $f_{b,org}$, but rather results from a direct coupling between Earth's carbon and oxygen cycles such that oxygen release from organic carbon burial ultimately controls the average $\delta^{13}C$ value of carbon entering the ocean-atmosphere system. As noted above, mass balance in the system in maintained by allowing for organic carbon deposited in marine sediments to not be recycled back into the surficial carbon cycle (allowing for the presence of detrital petrogenic organic carbon or organic carbon subduction). There are relatively poor constraints on atmospheric pO_2 levels in the Paleoproterozoic during the so-called Lomagundi carbon isotope excursion. According to the traditional framework, this positive carbon isotope excursion requires extremely high rates of organic carbon burial ($f_{b,org} > 0.5$) (for example (Kump and Arthur, 1999)). Conversely, if low atmospheric oxygen levels (for example $pO_2 < 5\%$ PAL) were sustained through this interval, moderate (that is, less than modern) rates of organic carbon burial are possible (Fig. 13, 14). However, maintaining low atmospheric pO_2 levels with near modern rates of organic carbon burial during the Lomagundi interval would require fundamentally different oxygen sinks than in the modern (see Kasting and Canfield, 2012; Laakso and Schrag, 2014). Progressive oxidation during tectonic recycling of a ferrous iron-rich upper continental crust that formed during the Archean is one potentially significant oxygen sink that is unique to the Paleoproterozoic (see Kump and Holland, 1992; Bachan and Kump, 2015).

Alternative views of the carbon isotope mass balance

There are several recently discussed processes that we have not incorporated into our carbon isotope mass balance. We do not include authigenic carbonates in our mass balance.

669 Previous work suggest that there would be increased burial of isotopically depleted carbonate in an
670 anoxic ocean, allowing for the reduction in organic carbon burial while keeping marine DIC values
671 near 0‰ (Schrag and others, 2013). More specifically they suggested greater extents of anaerobic
672 remineralization (sulfate and iron reduction) in Precambrian oceans would trigger more authigenic
673 carbonate formation (Schrag and others, 2013). Although intriguing, potential issues have arisen
674 with the 'authigenic carbonate hypothesis' (for example Li and others, 2015, Shields and Mills,
675 2017). For instance, with a very large marine sulfate reservoir and with extensive bioturbation
676 linked sulfide and ferrous iron reoxidation the modern oceans likely sustain much higher extents
677 of iron and sulfate reduction than the Precambrian oceans could have—and thus in the suggested
678 framework, the modern oceans should be primed for authigenic carbonate burial, but this is
679 estimated to be a relatively minor term (Schrag and others, 2013; Sun and Turchyn, 2014). In
680 Precambrian marine settings reoxidation was limited—with no bioturbation—and sulfate
681 concentrations are typically thought to have been very low (<1mM) relative to modern oceans (28
682 mM) (Fakhraee and others, 2019). Further, Precambrian and Phanerozoic authigenic carbonates
683 typically have only slightly depleted $\delta^{13}C_{carb}$ values (< -5‰), in part because of precipitation of
684 isotopically heavy carbonate in methanic zone (Sun and Turchyn, 2014). If authigenic carbonates
685 on average have $\delta^{13}C$ values < -5‰, they are unlikely to play a major role in the global carbon
686 isotope mass balance. Therefore, although authigenic carbonates are certainly locally important,
687 we feel this process is far less likely to lead to deviations in our traditional view of the global carbon
688 isotope mass balance than major shifts in $\delta^{13}C_{input}$ values. Therefore, with the current state of
689 knowledge, having variable $\delta^{13}C_{input}$ values through time provides a more compelling solution to
690 the paradox of constant $\delta^{13}C_{carb}$ values at varying oxygen levels. Similarly, there are several
691 problems with the large-scale sequestration of isotopically light carbon in hydrothermal systems
692 (Bjerrum and Canfield, 2004). Importantly, claims of a strong water column carbon isotope
693 gradient in the Precambrian oceans have been strongly refuted by several detailed carbon isotope
694 studies that have a sound sedimentological context (for example Fischer and others, 2009). Further,
695 a case can be made that there is no first-principle geophysical or geochemical evidence for more
696 rapid plate tectonics and more vigorous hydrothermal exchange early in Earth's history (for
697 example Korenaga, 2013), despite a hotter mantle, which had been invoked to account for more
698 hydrothermal carbonate removal. Lastly, we have not explicitly included a methane flux or included
699 large methane fluxes in low oxygen systems. However, following Kump and Arthur (1999), we
700 have included an offset in the isotopic composition of 'fresh' and 'fossil' organic matter that
701 accounts for loss of light carbon (for example methane) during diagenesis and have assumed a
702 negative-$\delta^{13}C$ metamorphic and volcanic outgassing term despite the potential preferential
703 carbonate relative to organic degassing during metamorphism. This approach is likely conservative,

for our purposes, as methane fluxes will scale with organic matter burial and thus should be minor in low productivity systems (see below). Further, there is no evidence for a switch to markedly heavy organic carbon isotope values in low oxygen systems (Krissansen-Totton and others, 2015), which would be a signature of a significant mass transfer of organic carbon to inorganic carbon via methane generation and oxidation.

Results of the marine 1D steady-state reactive-transport model

We find that the burial efficiency (BE) is mainly controlled by oceanic oxygen concentration, which is calculated from the suggested atmospheric oxygen trajectory through time (Lyons and others, 2014) (fig. 15). The efficiency of the carbon pump is high in anoxic Archean oceans and drops below 20% during the Proterozoic, owing to efficient carbon degradation in oxic shallow waters, and decrease to the modern value (<1%) during Phanerozoic, where deep water became fully oxygenated. We note that this is only an illustrative reconstruction of the evolution of surface oxygen levels (there are intervals in the Proterozoic when there was likely widespread oxic conditions and interval of the Phanerozoic where the deep oceans were likely not oxic). These trend in burial efficiency simply builds on the organic matter degradation being more efficient in oxic than anoxic conditions, which has been a key part of conceptual and quantitative models of ocean biogeochemistry (Middelburg, 1989; Arndt and others, 2013; Katsev and Crowe, 2015). Specifically, the trend is a result of our utilized revised carbon degradation rate law proposed by Katsev and Crowe (2015) which is based on a well-established rate law suggested by Middelburg (Middelburg, 1989), but that accounts for higher rate of carbon degradation under oxic conditions.

Strong shifts in the efficiency of the carbon pump, tightly linked to atmospheric oxygen level and $F_{b,org,}$ lea to extensive fluctuation in marine net primary production (NPP) over time (fig. 16; see also Laakso and Schrag, 2014). Notably, high burial efficiency and suppressed terrestrial organic matter oxidation under an anoxic atmosphere ($pO_2 < 10^{-5}$ PAL) during the Archean results in a small biosphere with estimated average oxic net primary production of 4.8 ± 1.25 Tmol/year (mean ± σ), which is more than three orders of magnitude lower than the modern NPP (fig. 16). It is important to note that there could be a massive biosphere dependent on iron redox cycling that would not be included in these numbers. After the GOE assuming an oxygen overshoot period during the Lomagundi excursion, net primary production could have reached modern values (1330 ± 2870 Tmol/year (mean ± σ)) due to efficient cycling of nutrients within the ocean (Kipp and Stüeken, 2017) (low burial efficiency) under oxygenated conditions ($pO_2 > 0.01$ PAL), which is reflected in high a high value for $f_{b,org}$ (fig. 16). However, we stress these estimates are strongly

dependent on an assumed pO_2 and there are currently few constraints and no consensus about Paleoproterozoic atmospheric oxygen levels. The mid-Proterozoic, marks a significant drop in the marine net primary production (84 ± 35 Tmol/year), owing to diminished terrestrial organic matter oxidation and high burial efficiency under low atmospheric oxygen levels (pO_2 < 0.1 PAL; fig. 16). Deepwater oxygenation at the dawn of the Phanerozoic would have promoted the maximum oxidation of organic matter on land and efficient nutrient cycling (extremely low burial efficiency) in the ocean, which collectively, would have shaped a modern biosphere (mean NPP = 5014 ± 4736 Tmol/year) (fig. 16). It is important to note we have not assumed a rise in oxygen associated with the rise of land plants—and this assumption leads to relatively constant NPP over the Phanerozoic.

Sensitivity analysis of the marine 1D steady-state reactive-transport model

We conducted a range of parameter sweeps to investigate the sensitivity of our 1D steady-state reactive-transport model (Table A5). Results from the sensitivity analysis indicate that the value of burial efficiency (BE) is relatively insensitive (<15% relative change in BE) to most parameters including a reasonable range of settling rate of oceanic aggregates, cf. figure A5 (Alonso-Gonzalez and others, 2010; McDonnell and Buesseler, 2010). Assuming roughly constant background surface temperatures, the parameters that most strongly impact the efficiency of the biological carbon pump are turbulent diffusion coefficients, changes in atmospheric oxygen level, and iron oxidation rate constant. Notably, by enhancing the rate of organic matter degradation, increased ocean-atmosphere oxygen concentrations result in deeper oxygen penetration and a more inefficient carbon pump (more efficient nutrient recycling). Increasedd in oxygen diffusivity would also lead to a deeper oxygen penetration depth (OPD), resulting in a more inefficient carbon pump. An order of magnitude increase in the surface water turbulent diffusion coefficient (more vigorous ocean circulation) would result in more than 35% decrease in the burial efficiency. This effect is more pronounced at the surface water where a high rate of organic matter degradation occurs (fig. A5). By impacting the oxygen consumption and modulating OPD, an increased iron oxidation rate constant would result in shallower OPD and higher burial efficiency.

DISCUSSION

Given virtually any currently widely accepted reconstruction of atmospheric O_2 levels (for example Lyons and others, 2014), a constant baseline in $\delta^{13}C_{carb}$ values near 0‰ suggests there has been a secular increase in organic carbon burial rates through time. More specifically, our analysis suggests there were intervals of time (the Archean and the mid-Proterozoic) where organic carbon burial rates were lower than the modern despite similar baseline carbonate carbon isotope values

775 (Fig. 12, 13). Because organic carbon burial is generally more efficient in the reducing marine
776 environments that were pervasive in the Precambrian, the most obvious mechanism for
777 dramatically reducing organic carbon burial—required to satisfy isotope mass balance given our
778 revised f_{org} estimates for a low-oxygen Precambrian world—is to reduce nutrient availability for
779 oxygenic phototrophs (see Derry, 2014; 2015). There are several scenarios whereby a largely
780 anoxic ocean—a consequence of low atmospheric pO_2—would be expected to trigger a nutrient
781 crisis (Bjerrum and Canfield, 2002; Fennel and others, 2005a; Laakso and Schrag, 2014; Derry,
782 2015; Reinhard and others, 2017). Foremost, there is likely to be enhanced abiogenic phosphorous
783 scavenging in an anoxic ocean (Bjerrum and Canfield, 2002; Derry, 2015; Reinhard and others,
784 2017). Consistent with this view, a fundamental shift in the P cycle roughly coincident with
785 Neoproterozoic oxygenation was proposed based on a record of P burial in marine sediments
786 (Reinhard and others, 2017). Additionally, at higher atmospheric oxygen levels, more extensive
787 carbon oxidation will lead to enhanced acidity, which will fuel apatite dissolution during
788 weathering (Guidry and Mackenzie, 2000). The extent of acid generation is a key aspect controlling
789 global P fluxes, given that significant detrital apatite moves through the weathering realm (Guidry
790 and Mackenzie, 2000; Jaisi and Blake, 2010). The soil acid fluxes from petrogenic organic carbon
791 oxidation are comparable to pyrite oxidation, albeit much smaller than contemporary soil organic
792 matter oxidation (for example organic matter degradation in the O horizon of soils) and may drive
793 a shift in phosphorous fluxes from soils. Regardless of the mechanisms controlling the evolution
794 of P cycling, our updated framework for the global carbon cycle supports the notion of strong
795 nutrient limitation through much of Earth's history (cf., Derry, 2014, Laakso and Schrag, 2014).
796
797 Extensive variability in $F_{b,org}$ and atmospheric oxygen level is consistent with significant
798 variability in the size of the biosphere. The first major rise of atmospheric oxygen, the GOE, is
799 thought to have culminated in an oxygen overshoot during the Lomagundi. Enhanced organic
800 matter oxidation on land, along with efficient nutrient cycling in oxygenated oceans due to low
801 burial efficiency, would have resulted in increased marine NPP—potentially even similar to the
802 modern. However, we still have very poor constraints on atmospheric oxygen levels during this
803 time interval. The potential for a large drop in atmospheric oxygen levels in the mid-Proterozoic
804 (for example Shen and others, 2003; Planavsky and others, 2014; Tang and others, 2016) would
805 have decreased organic matter oxidation on land, and increased burial efficiency in the ocean. This
806 system would only be stable with lower marine NPP (for example Laakso and Schrag, 2014; Ozaki
807 and others, 2019). Intriguingly, this conclusion is potentially supported by recent results from
808 oxygen isotopes in sulfate evaporites. Specifically, results from analyses of $\Delta^{17}O$ in
809 Paleoproterozoic sulfate minerals suggest a dramatic decline in either primary productivity and/or

atmospheric oxygen at the end of the Lomagundi (~2000 Ma; Hodgskiss and others, 2019). These sulfate minerals are marked with relatively large negative triple-oxygen isotope anomalies (as low as ~ −0.8‰). Such negative values, which would have occurred shortly after the Lomagundi, can be explained by a drastic reduction in primary productivity of 80% or more (Hodgskiss and others, 2019). However, it is important to note that we are still working out several even basic aspects of the Precambrian $\Delta^{17}O$ record (for example Liu and others, 2021). A smaller biosphere may have persisted for much of the Proterozoic, until deep ocean oxygenation and the second rise of atmospheric oxygen at end of Proterozoic, referred to as Neoproterozoic oxidation event (NOE). Finally, the rise of a modern-like marine (and, or terrestrial) biosphere would have led to extents of organic matter oxidation on land that are comparable to the modern under a well-oxygenated atmosphere and efficient nutrient cycling in the well-oxygenated oceans.

Coupled variability in $\delta^{13}C_{input}$ values, petrogenic organic carbon oxidation, and atmospheric pO_2 levels provides a simple and mechanistically robust explanation for long-term carbon isotope stasis that does not invoke constant organic burial fluxes (see also Daines and others, 2017). However, this view does not imply that the amount of oxygen released to the atmosphere and the extent of organic carbon oxidation will be exactly balanced. With this framework, there is oxygen release to the atmosphere even at low pO_2 (Fig. 9). In a low oxygen world this release can be largely consumed by reaction with metamorphic and non-organic sedimentary reductants (leading to more limited petrogenic organic carbon oxidation). Daines and others (2017) built from this idea—by reinterpreting the carbon isotope record in light of organic oxidation model results—to propose that there would be a minimum stable atmospheric oxygen levels for the Proterozoic. The core idea is that with lower atmospheric oxygen levels—where there are lower extents of petrogenic organic carbon oxidation—isotope mass balance dictates there will be lower organic carbon burial fluxes (and thus lower oxygen fluxes). At some critical pO_2, this oxygen flux will be lower than the volcanogenic gas flux, which would result in an anoxic, Archean-like atmosphere. Our analysis supports that this idea is fundamentally sound. Daines and others (2017), further, proposed that this critical pO_2 threshold was likely between >1 and <10% PAL, with a preferred model value of roughly 5% PAL. Our sensitivity analysis (Fig. 9, 13) highlights the difficulties in pinpointing the exact atmospheric oxygen level at which this transition occurs—regardless of uncertainties in magnitude reduced gas fluxes. We found that the Earth system could 'stabilize' at a pO_2 anywhere from roughly 0.1% to 10% PAL. In other words, the oxygen flux could exceed estimated reduced gas fluxes (~2500 Tm/kyr; as low as 1000 Tm/kyr; as high as 4000 Tm/kyr; Daines et al., 2017) over a wide range of atmospheric oxygen levels (roughly 0.1% to 10% PAL). However, what we consider the most reasonable estimates with this framework—ones that include

transport oxidation—suggest that pO_2 may stabilize around 1% PAL with mean reduced gas estimates (see Fig. 9, 13). Further, it is important to stress that we are not presenting a full sensitivity analysis—for instance varying soil porosity and tortuosity can also lead to enhanced organic carbon oxidation at low atmospheric oxygen levels. With that in mind, we think there are two takeaways from our analysis of the effects of organic carbon oxidation on the long-term carbon cycle. One, even with more realistic parameterizations of organic matter and erosion rate distributions, there is strong support that the extents of organic carbon oxidation are likely to vary substantially with the atmospheric oxygen levels predicted from the Proterozoic and Phanerozoic. Two, this modification of the traditional view of the carbon isotope record (*cf.* Derry, 2014) is unlikely to provide a pO_2 estimate that will allow us to distinguish between different proxy records.

Critically the idea that organic carbon oxidation has changed dramatically though time makes the empirically testable prediction that there should be significant detrital organic matter in Precambrian sedimentary rocks. Recently, decoupling of carbonate and organic carbon isotope values in the Neoproterozoic has been used to argue for the presence of detrital organic matter (Johnston and others, 2012). There is also evidence for organic and carbonate carbon isotope decoupling during the Paleoproterozoic (Bekker and others, 2008), which could also be linked to the presence of detrital organic matter. Unfortunately, this direct test of our model cannot be applied to most of the Precambrian sedimentary record, given limited $\delta^{13}C_{carb}$ variability. However, it might be possible to empirically test our hypothesis by using alternative petrographic approaches (for example (Raman spectroscopy on sedimentary organic material) to examine whether there may have been significant detrital organic material moving through Earth surface environments at specific time intervals (Marshall and others, 2009; Canfield and others, 2021). However, this approach relies heavily on limited thermal maturation of the analyzed organic matter and a high degree of initial thermal maturation of the detrital organic matter. Therefore, there are likely large uncertainties associated with any interpretations of sedimentary organic composition data from single, or a limited number, of settings (see also Canfield and others, 2021). Further, as highlighted in part by our sensitivity analyses, there are significant sources of uncertainties in linking an extent of organic carbon oxidation to the atmospheric oxygen levels (for example variable uplift and denudation rate; varying extents of post-soil formation oxidation). Nonetheless, following this approach in modern through Precambrian sedimentary settings (Canfield and others, 2021) is a promising means tracking the history of sedimentary organic carbon oxidation.

CONCLUSION

In this study, we explored the link between atmospheric oxygen level, organic matter oxidation in terrestrial systems, and marine net primary production. Our modeling results indicate a major role of atmospheric oxygen in governing the long-term carbon burial in the ocean. Notably, our modeling results lend credence to the fact that the fraction of carbon buried as organic matter (f_{org}) has extensively fluctuated throughout Earth's history (supporting Derry, 2014; Daines et al., 2017. We propose that the carbonate carbon isotope record has been characterized by a relatively constant baseline value over time due to a fundamental mechanistic link between atmospheric O_2 levels and the carbon isotopic composition of net inputs to the ocean-atmosphere system. We further show that extensive variability in the burial flux of organic carbon ($F_{b,org}$) and atmospheric oxygen level suggests dramatic fluctuation in marine net primary production (NPP) through time. This variability in marine NPP is linked to changes in organic matter oxidation on land and changes in the efficiency of the carbon pump in the oceans, both of which are tightly linked to variations in atmospheric oxygen level. This view of the global carbon cycle is consistent with an emerging model of strong nutrient limitation, relative to the modern, for most of Earth's history.

Acknowledgements:

NJP, EWB, CTR, YTT were funded through the Alternative Earths NASA Astrobiology Institute and EWB received support from Virtual Planetary Laboratory through the NASA Astrobiology Institute. We thank the editor, P. Chamberlain, D. Ibarra and the other anonymous reviewer for providing us with insightful comments and suggestions. NJP acknowledges support from the Packard Foundation. EWB would like to thank Jules E. Bolton for discussions regarding statistics and distributions, and Mark Brandon for discussion of erosion rates. The developer (edward.bolton@yale.edu) of the research code developed for this study will make the FORTRAN code, sample input files, and R code used to calculate all quantities for the figures available upon reasonable request.

Appendix:

Formulation of the model for oxidation of organic matter and pyrite in a soil layer

This model description is modified from Bolton and others (2006), with permission. We have focused on a hypothetical state, where oxygen diffuses through interconnected pores. We ignore CO_2 (that would primarily be diffusing upward) and assume the air in the pore spaces is essentially stagnant. Equations describing oxygen diffusion and reaction, as well as the uplift and reaction of the reduced solids are:

$$\frac{a}{t} = \frac{1}{a}\frac{}{x}\left[{}_{a}D_{s}\frac{a}{x}\right] \div \sum_{i} \left[\frac{{}_{i}v_{i}}{a}\right] \div \tag{A1}$$

$$\frac{g_i}{t} = \left[\frac{g_i}{x}\right]_{i} \tag{A2}$$

for each i. The subscript or superscript i indicates the grain type being oxidized. We used i =1 for OM and i = 2 for pyrite, but the model includes the possibility of multiple grain size bins, each with their own characteristic kinetics and initial sizes. A summary of the variables in these equations, as well as the formulation of how the effective diffusion coefficient is related to the tortuosity are presented in Bolton and others (2006). We also define:

$${}_{i} = \frac{c_i R^{i}_{max} a g_i}{d_i \left(K^{i}_{m} + a \right)} \tag{A3}$$

for Michaelis-Menten or Monod kinetics (Boudreau, 1997), and

$${}_{i} = \frac{A_i a^{n} g_i}{d_i} \tag{A4}$$

for power-law kinetics. All results were derived from the Michaelis-Menton kinetics for OM oxidation, except for Fig. S1 and S2, where we show results using the power law version of OM kinetics. Note that:

$$\frac{1}{a}\frac{}{x}\quad {}_{a}D_s\frac{a}{x}\div = D_s\frac{{}^{2}a}{x^2}+\frac{a}{x}\ \frac{D_s}{x}\div+\frac{a}{x}\ \frac{D_s}{a}\frac{a}{x}\div \tag{A5}$$

935
936
937 and that:

$$\frac{g_i}{d_i} = b_i g_i^{2/3} \tag{A6}$$

938
939 for our grain model. The conversion factor b_i, is used to adjust units (Bolton and others, 2006). We
940 have not included compaction in the model in a rigorous way, but the first-order effects of
941 compaction to limit excessive increases in porosity (that could accompany oxidation of large
942 quantities of OM and pyrite) are approximated by use of an upper limit "lid" on the air porosity.
943
944 We have used an effective diffusion coefficient based on air in interconnected pore spaces.
945 Effective transport of oxygen depends critically on the interconnectivity of the air in the pore
946 spaces. If the soil is completely water saturated, oxygen diffusion into the soil is severely limited,
947 due to the low diffusivity of oxygen in water. Even moving water is not very effective in
948 transporting oxygen downward, due to the low oxygen content of water in equilibrium with air.
949
950 Choice of model parameters

951 Key model parameters are discussed in Tables A1 and A2, along with conversion factors
952 in Table A3. Shape factors were assumed for different grain types and porosity increased as OM
953 and pyrite were consumed (as the volume fraction, surface areas, and grain thickness d_i of OM and
954 pyrite are calculated during oxidation, the implied change in porosity is also calculated). We have
955 limited the maximum allowed air porosity at a prescribed "lid" value (10%), as a simple way of
956 incorporating the most important effects of compaction that can serve to limit large porosity
957 increase. Increasing the porosity will increase the effective diffusion coefficient because the
958 porosity-dependent tortuosity factor increases. For OM, we assumed plate-like organic matter
959 particles with aspect ratio α_i = 5 (width and length)/(thickness d_i). This assumption is consistent
960 with SEM work (for example Ref. Wildman and others, 2004) and is more conservative (for the
961 purposes of this paper) than assuming nearly spherical grains. The model allows for dynamic
962 changes in grain size during oxidation—where surface area (a key factor in kinetic control) exposed
963 to oxidation decreases while the OM volume decreases. Rectangular platelets with width and length
964 L_i, thickness d_i, and $\alpha_i = L_i / d_i$, have surface areas of $2\alpha_i d_i^{\,2}(2+\alpha_i)$ and volumes $\alpha_i^{\,2} d_i^{\,3}$ per particle,

yielding an area to volume ratio of $2(2+\alpha_i)/(\alpha_i\, d_i)$ per particle. Pyrite is assumed to be euhedral. (the model used $\alpha_i = 1$). However, cubes will have a similar size, area, and volume scaling as for spheres with only a reactive outer layer. In terms of the volume fraction of OM or pyrite, the number of particles of type *i* in a 1 m^3 reference volume, per volume, is $\bar{N}_i = \phi_{i,solid}/(\alpha_i^2\, d_i^3)$, with units of number per m^3. $\phi_{i,solid}$ is the volume of *i* type grains per bulk volume. Given that sulfides are quantitatively oxidized over the majority of the parameter space explored, pyrite morphology has essentially no effect on the global carbon isotope mass balance calculations.

We used ν_i =1 for OM, and ν_i =15/4 for pyrite (appropriate for final end-products of oxidation). We used 15.171 g OM per mole of C in OM, as calculated from the assumed OM composition of $C_{40}H_{48}O_2N_1S_1$ (Petsch, 2000; Petsch and others, 2000). Values for the diffusion coefficient of oxygen and air were adopted as the same as *S1*, where $D_0 = 0.178 \bullet (cm^2/s) \bullet (T(K)/273.15)^{1.75}$ at a pressure of 1 atm. and 17ºC (mid latitude average).

There are partially compensating effects of faster reaction at higher temperatures, versus lower Henry's law fractionation at higher temperatures. However, we performed numerous model runs that indicated that the increase of reaction rates with temperature is slightly more pronounced than the decrease in rates arising from lower dissolved oxygen that accompany higher temperatures. Given the canceling effects with temperature rise, we have used a constant temperature (17ºC) for all of the modeling runs used for the carbon cycle modeling.

The rate of OM oxidation was based on the experimental study (Chang, 1997; Chang and Berner, 1998; Chang and Berner, 1999) of the kinetics of coal oxidation in aqueous solutions containing various measured quantities of dissolved oxygen. Coal was used given the difficulty of obtaining sulfur-free marine kerogen. We are forced to use coal given the lack an experimental study of the kinetics of kerogen oxidation in water. The relative oxidation rate of coal versus kerogen is not known, but the rates are probably similar despite differing initial organic compound compositions. See Bolton and others (2006) for a systematic sensitivity study regarding the variation of organic matter oxidation rates (and other key variables). Temperature dependence of the rate is accounted for using an apparent activation energy of 42 kJ/mole O_2 (Chang and Berner, 1999). $R_{max}^{CH:TEXP}$(mol *i* m^{-2} s^{-1}) is the maximum rate of the OM oxidation reaction, which can be related to the R_{max} parameter described above by:

$$R^{i}_{max}\ \frac{\text{mol } i}{\text{m}^2\text{y}} = R^{CH:TEXP}_{max}\ \frac{\text{mol } i}{\text{m}^2\text{s}} \times \left(3.15\text{x}10^{7}\ \text{s/yr}\right) \times \text{eactfact}_i \qquad \text{(A7)}$$

998

$$\text{eactfact}_i = \exp\ \frac{E_a(\text{J}/(\text{mol } i\ \text{rxn}))}{8.314(\text{J}/(\text{mol}\times\text{K}))} \times \frac{1}{T_{\exp}(\text{K})}\ \ \frac{1}{T_{sim}(\text{K})} \qquad \text{(A8)}$$

999

1000 where T_{sim} is the temperature of the simulation (in Kelvin) and T_{exp} is the temperature (K) of the
1001 experimentally derived kinetics, and E_a is the activation energy appropriate to capture the
1002 temperature dependence of the kinetic rate. From Petsch and others (2000) we used $R_{max}{}^{CH:TEXP}$ •
1003 $3.15\text{x}10^7$s/yr (mol i m^{-2} s^{-1}) = 1.015×10^{-4} (mole C or O_2 consumed/m^2/yr) and K_m = 1.787×10^{-6}
1004 (mole O_2/cm^3 air). There is a conversion between K_{wat} (if estimated from micromole O_2/Liter of
1005 water) and K, and Henry's law partitioning that is exploited to account for the difference between
1006 oxygen concentrations in the water and in the air. We fit the oxidation data with the Michaelis-
1007 Menten rate law fit used by Petsch and others (2000) and a power law fit. The square-root
1008 dependence fit used by Lasaga and Ohmoto (2002) underestimates the rate by about a factor of two
1009 for low oxygen levels compared to the other two fits.
1010
1011 Pyrite oxidation kinetics have been studied by numerous groups, including Smith and
1012 Shumate (1970), McKibben and Barnes (1986), Nicholson and others (1988) Williamson and
1013 Rimstidt (1994), Jerz and Rimstidt (2004), and Gleisner and others (2004). The influence of oxygen
1014 concentration on the rate of pyrite oxidation was examined by Smith and Shumate (1970), whose
1015 abiotic rate data is nicely modeled using a power law fit for pyrite oxidation with $A_{pow:Texp}$ (rate of
1016 pyrite oxidation (in mole pyrite consumed/m^2/s) =2.013×10^{-12} × [O_2 in water in micromole/ L]$^{0.6696}$.
1017 Although Smith and Shumate (1970) do not report the pH for the runs our calculations suggest the
1018 pH must have been in the range of 3 to 5, and we expect reasonably low pH for the sediment waters
1019 in contact with pyrite. This roughly 2/3 power law dependence on oxygen concentration was not
1020 noted in any of the papers cited above. The influence of microbial activity was found to increase
1021 rates of oxidation by up to almost an order of magnitude. Biotic and abiotic oxidation data were
1022 studied by Gleisner and others (2004), whose abiotic kinetic rates nearly match the abiotic rate
1023 found by Smith and Shumate. Smith and Shumate also measured some biotically controlled rates,
1024 with similar kinetic acceleration. Conversion of the power law form above to the factor A_i is
1025 described in Table A3. The sensitivity of other parameters is shown in Bolton and others (2006),
1026 where, initial porosity was varied from 2 percent to 10 percent, tortuosity exponent from n*=0.5 to
1027 n*=2, and grain thickness from 5 to 20 microns.

The mean global physical denudation rate today is 8.5 cm/kyr with mean values for continents ranging within a factor of ten (Berner and Berner, 2012). This value should also apply to shales. The present global denudation rate is about two times higher than the past, due to the effect of human activity (mainly agriculture) on erosion (Berner and Berner, 2012). About 4.2 cm/kyr is then appropriate for physical denudation of shales in the pre-agricultural earth. This rate reflects only eroded material that is delivered to the sea. Much eroded material is deposited in valleys, hollows, lowland soils, *et cetera*, and is subjected to additional oxidative weathering of any transported organic carbon during storage (see Blair and others, 2004). Below we explore the sensitivity of the carbon cycle modeling to OM oxidation in overbank and similar deposits. This 4.2 cm/kyr estimate is close to the 5 cm/kyr used by Lasaga and Ohmoto (2002). We varied mean denudation rates from 1.19 to 500 cm/kyr in the present study. Atmospheric oxygen levels were set as some fraction of the present level (20.9476% by volume, or by moles), (with 1 PAL corresponding to the present atmospheric level). Higher erosion rates are present in areas with extreme elevation, making our approach, for the purposes of this paper, conservative. We describe the utilized denudation rate distributions below.

The extent of organic carbon in the upper continental crust is likely to change through over time on tectonic recycling time scales. However, for the steady state carbon cycle calculations in this paper we used previous estimates of the average upper continental crust. Holland's (1978) summary of average shale compositions range from 0.69 to 0.94 mass per cent of organic carbon (see also Raiswell and Berner, 1986). We describe the utilized initial organic matter distributions below.

Conversion factors

We give conversion factors between mass fractions, and the concentrations g_i for the cases of i corresponding to pyrite or C in OM. For volume fractions and densities, type i corresponds simply to pyrite or OM (not C in OM). See Table A3. The concentration g_i is related to MF_i, the mass fraction of i in the dry "rock", by:

$$g_i\left[\frac{\text{mole pyrite or C in OM}}{\text{cm}^3\ \text{bulk}}\right]=\left(\frac{MF_i\left[\frac{\text{g pyrite or C in OM}}{\text{g dry rock}}\right]\cdot\left(\rho_{solid}\left[\frac{\text{g solid}}{\text{cm}^3\ \text{solid}}\right]\right)}{MW_i\left[\frac{\text{g type } i}{\text{mole type } i}\right]\cdot\left(\frac{1}{B,solid}\left[\frac{\text{cm}^3\ \text{bulk}}{\text{cm}^3\ \text{solid}}\right]\right)}\right) \qquad \text{(A9)}$$

Note that the total organic carbon mass fraction (TOC) is just MF_i for the appropriate i. To convert between volume fraction and concentration, we use:

$$_{i,solid}\left[\frac{\text{cm}^3 \text{ pyrite or OM}}{\text{cm}^3 \text{ bulk}}\right]=\left(\frac{g_i\left[\frac{\text{mole pyrite or C in OM}}{\text{cm}^3 \text{ bulk}}\right]\cdot gtim_i\left[\frac{\text{g pyrite or OM}}{\text{mole pyrite or OM}}\right]}{_i\left[\frac{g \text{ pyrite or OM}}{\text{cm}^3 \text{ pyrite or OM}}\right]\cdot\left(\frac{1 \text{ mole pyrite or C in OM}}{1 \text{ mole pyrite or OM}}\right)}\right) \qquad \text{(A10)}$$

The 15.171 g OM/(mole OM) comes from the assumption that 1 mole of OM contains 1 mole of C and corresponds to the element ratios $(C_{40}H_{48}O_2N_1S_1)\div 40 \rightarrow C_1H_{1.2}O_{0.05}N_{0.025}S_{0.025}$, whose molecular weight is 15.171g OM/(mole OM). $\phi_{i,solid}$ is the volume fraction of particles of type i (OM or pyrite) in the bulk.

To convert between volume fraction and mass fraction, we use:

$$_{i,solid}\left[\frac{\text{cm}^3 \text{ pyrite or OM}}{\text{cm}^3 \text{ bulk}}\right]=\left(\frac{MF_i\left[\frac{\text{g pyrite or C in OM}}{\text{g dry rock}}\right]\cdot\left(_{solid}\right)\cdot{}_{B,solid}}{gtig_i\left[1\frac{\text{g } FeS_2}{\text{g pyrite}} \text{ or } 0.7916\frac{\text{g C in OM}}{\text{g OM}}\right]\cdot{}_i}\right) \qquad \text{(A11)}$$

The factor 0.7916 corresponds to (12.01 g C/(mole OM)) ÷(15.171 g OM/(mole OM)).

We now give the forms of other factors needed to convert units.

b_i = a conversion factor to adjust units, where:

$$b_i=\left(\frac{\bar{N}_i{}_i^2{}_i}{gtim_i}\cdot\left(\frac{1 \text{ mole pyrite or C in OM}}{\text{mole pyrite or OM}}\right)\right)^{1/3} \qquad \text{(A12)}$$

α_i is a shape factor discussed above. The conversion factor in the reaction term is:

$$c_i=\left(\frac{2(2+{}_i)}{{}_i}\left(\frac{1 \text{ m}^3}{10^6\text{cm}^3}\right)\frac{gtim_i}{{}_i}\right) \qquad \text{(A13)}$$

where ρ_i is in cgs units, and the m/cm conversion is required by the fact that d_i is in units of meters.

For cases using power-law kinetics we fit the form $A_{pow:Texp}$ *({O2})^n to experimental data. The parameter $A_{pow:Texp}$ is used for the power-law prefactor at the temperature of the experimental measurements, and has the units appropriate to make $\mathcal{R}_i$ with units described in Table A1. We used experimental data for oxidation rates that are in units of [(mole pyrite or C in OM consumed)/(m^2 exposed pyrite or OM surface area)/s] and experimental measurements of the oxygen concentration in micromole of O_2/Liter of water: ({O2}). This must be subsequently converted into different units given the form and units of A_i in our governing equations and the fact that the experimental data used oxygen concentrations in water, but our final power-law form uses oxygen concentrations in the gas phase, so the Henry law partitioning must also be taken into account, through "convptc". This leads to the following: $A_i = A_{pow:Texp}$ *(3.15×10^7 s/yr) * eactfact$_i$*c_i*(convptc)^n, with convptc defined below.

When converting K_{wat} to K_m we have: $K_m = K_{wat}$ /convptc with:

$$\text{convptc} = (10^6 \frac{\text{micromole}}{\text{mole}}) \cdot (10^3 \frac{\text{cm}^3}{\text{Liter}}) \cdot (10^6 \frac{\text{cm}^3}{\text{m}^3}) \cdot \cdot (\frac{_{\text{wat}}\left[\text{g/cm}^3\right]}{\text{M}_{\text{wat}}\left[\text{g/mole}\right]}) \cdot (\frac{\text{R}\left[\text{J/mole/K}\right] \cdot \text{T}\left[\text{K}\right]}{\text{P}_{\text{atm}}\left[\text{Pascals}\right]}) \cdot X_1 \qquad \text{(A14)}$$

The mole fraction of O_2 in water is X_1*(partial pressure of O_2 in air, which for a total pressure of 1 atm is the volume fraction of O_2 in air), with X_1 from Gevantman (2006). M_{wat} is the molecular weight of water. For a total pressure of 1 atm, the partial pressure of O_2 in air (in atm) is numerically equal to the volume fraction of O_2 in air.

Numerical methods

We used an implicit finite-difference method to solve the presented equations. Some difficulties arise in the equations given above due to the "stiff" nature of the equations (cf. Bolton and others, 2006). During a transient phase of the solution, as the system is evolving toward steady state, the reaction terms may be much larger than the advection and diffusion terms. As the system comes close to steady state, a balance develops between advection (erosion bringing up fresh material) and reaction for the pyrite and OM equations, while a balance of reaction with diffusion terms develops in the oxygen equation. For equivalent surface areas and oxygen concentrations,

1116 the oxidation rate of pyrite is at least an order of magnitude higher than that of the OM. The
1117 numerical solutions obtained for typical OM and pyrite "grain" sizes and shapes leads to "fronts"
1118 that are much sharper for pyrite than for OM. Components of the system may essentially disappear
1119 in some locations (oxygen at depth, pyrite and OM near the surface), necessitating the use of
1120 thresholds in the code below which one must assume a complete absence.

1121

1122 The complete description of the numerical method is given in Bolton and others (2006).
1123 To solve the governing equations (equations A1, A2, A5) the equations have been written in their
1124 finite difference form. Within each time step, iterations are performed (typically two sub-time-step
1125 iterations). Care is taken with the reaction term to avoid underflow and overflow when values of *a,*
1126 *d*, or *g* become very small. Reaction terms are zeroed out if the size of the grains had $d_{i,j} < 1$nm or
1127 if $a_j < 10^{-40}$ mole O_2/cm^3 air. Additionally, special forms of the finite difference expressions given
1128 above are required at the top and bottom boundaries of the 1D computational domain, to
1129 accommodate boundary conditions. The equation for *a* was solved by transferring estimated values
1130 for the *a* terms to the left-hand side, while values depending on old values or previous iterations
1131 were placed on the right-hand side of a system that was solved by a tridiagonal algorithm. After the
1132 *a* equation was solved, the g_i equations were solved using the old and new time-step values of *a* for
1133 the reaction terms in an identical form as used in the *a* equation (with proper adjustment for the
1134 stoichiometry and porosity).

References:

Alonso-Gonzalez, I. J., Aristegui, J., Lee, C., Sanchez-Vidal, A., Calafat, A., Fabres, J., Sangra, P., Masque, P., Hernandez-Guerra, A., and Benitez-Barrios, V., 2010, Role of slowly settling particles in the ocean carbon cycle: Geophysical Research Letters, v. 37.

Arndt, S., Jørgensen, B. B., LaRowe, D. E., Middelburg, J. J., Pancost, R. D., and Regnier, P., 2013, Quantifying the degradation of organic matter in marine sediments: A review and synthesis: Earth-Science Reviews, v. 123, p. 53–86.

Bekker, A., Holmden, C., Beukes, N. J., Kenig, F., Eglingtone, B., and Patterson, W. P., 2008, Fractionation between inorganic and organic carbon during the Lomagundi (2.22-2.1 Ga) carbon isotope excursion: Earth and Planetary Science Letters, v. 271, p. 278–291.

Berner, R. A., Beerling, D. J., Dudley, R., Robinson, J. M., and Wildman, R. A., 2003, P HANEROZOIC A TMOSPHERIC O XYGEN : Annual Review of Earth and Planetary Sciences, v. 31, p. 105–134.

Bjerrum, C. J., and Canfield, D. E., 2002, Ocean productivity before about 1.9 Gyr ago limited by phosphorus adsorption onto iron oxides: Nature, v. 417, p. 159–162.

Bjerrum, C. J., and Canfield, D. E., 2004, New insights into the burial history of organic carbon on the early Earth: Geochemistry, Geophysics, Geosystems, v. 5.

Bluth, G. J. S., and Kump, L. R., 1991, Phanerozoic paleogeology: American Journal of Science, v. 291, p. 284–308.

Bolton, E. W., Berner, R. A., and Petsch, S. T., 2006, The weathering of sedimentary organic matter as a control on atmospheric O2: II. Theoretical modeling: American Journal of Science, v. 306, p. 575–615.

Canfield, D. E., 2005, THE EARLY HISTORY OF ATMOSPHERIC OXYGEN: Homage to Robert M. Garrels: Annual Review of Earth and Planetary Sciences, v. 33, p. 1–36.

Canfield, D. E., van Zuilen, M. A., Nabhan, S., Bjerrum, C. J., Zhang, S., Wang, H., and Wang, X., 2021, Petrographic carbon in ancient sediments constrains Proterozoic Era atmospheric oxygen levels: Proceedings of the National Academy of Sciences of the United States of America, v. 118, p. 2021.

Chang, S., and Berner, R. A., 1999, Coal weathering and the geochemical carbon cycle: Geochimica et Cosmochimica Acta, v. 63, p. 3301–3310.

Crowe, S. A., Døssing, L. N., Beukes, N. J., Bau, M., Kruger, S. J., Frei, R., and Canfield, D. E., 2013, Atmospheric oxygenation three billion years ago:

Daines, S. J., Mills, B. J. W., and Lenton, T. M., 2017, Atmospheric oxygen regulation at low Proterozoic levels by incomplete oxidative weathering of sedimentary organic carbon: Nature Communications, v. 8.

1170 Derry, L. A., 2015, Causes and consequences of mid-Proterozoic anoxia: Geophysical Research
1171 Letters, v. 42, p. 8538–8546.
1172 Dixon, J.L., and F. von Blanckenburg, 2012, Soils as pacemakers and limiters of global silicate
1173 weathering, Compes Rendus Geoscience, 344, 597–609.
1174 Fakhraee, M., Hancisse, O., Canfield, D. E., Crowe, S. A., and Katsev, S., 2019, Proterozoic
1175 seawater sulfate scarcity and the evolution of ocean–atmosphere chemistry: Nature
1176 Geoscience, v. 12, p. 375–380.
1177 Fakhraee, M., Planavsky, N. J., and Reinhard, C. T., 2020, The role of environmental factors in the
1178 long-term evolution of the marine biological pump: Nature Geoscience, v. 13, p. 812–816.
1179 Fakhraee, M., Tarhan, L. G., Planavsky, N. J., and Reinhard, C. T., 2021, A largely invariant marine
1180 dissolved organic carbon reservoir across Earth's history: Proceedings of the National
1181 Academy of Sciences of the United States of America, v. 118.
1182 Fennel, K., Follows, M., and Falkowski, P. G., 2005, The co-evolution of the nitrogen, carbon and
1183 oxygen cycles in the proterozoic ocean: American Journal of Science, v. 305, p. 526–545.
1184 Fischer, W. W., Schroeder, S., Lacassie, J. P., Beukes, N. J., Goldberg, T., Strauss, H., Horstmann,
1185 U. E., Schrag, D. P., and Knoll, A. H., 2009, Isotopic constraints on the Late Archean
1186 carbon cycle from the Transvaal Supergroup along the western margin of the Kaapvaal
1187 Craton, South Africa: Precambrian Research, v. 169, p. 15–27.
1188 Fritsch, F. N., and Carlson, R. E., 1980, Monotone Piecewise Cubic Interpolation: SIAM Journal
1189 on Numerical Analysis, v. 17, p. 238–246.
1190 Guidry, M. W., and Mackenzie, F. T., 2000, Apatite weathering and the Phanerozoic phosphorus
1191 cycle: Geology, v. 28, p. 631–634.
1192 Hayes, J. M., 2019, Fractionation of carbon and hydrogen isotopes in biosynthetic processes, in
1193 Stable Isotope Geochemistry: De Gruyter Mouton, p. 225–277.
1194 Hayes, J. M., and Waldbauer, J. R., 2006, The carbon cycle and associated redox processes through
1195 time: Philosophical Transactions of the Royal Society B: Biological Sciences, v. 361, p.
1196 931–950.
1197 Hodgskiss, M. S. W., Crockford, P. W., Peng, Y., Wing, B. A., and Horner, T. J., 2019, A
1198 productivity collapse to end Earth's Great Oxidation: Proceedings of the National
1199 Academy of Sciences, p. 201900325.
1200 Holland, H. D., 1978, The chemistry of the atmosphere and oceans - (v. 1):
1201 Holland, H. D., 1984, The chemical evolution of the atmosphere and oceans: Princeton University
1202 Press, 582 p.
1203 Holland, H. D., 1985, The Chemical Evolution of the Atmosphere and Oceans: Geological
1204 Magazine, v. 122, p. 404–405.

Horwath, W. R., 2006, The Phanerozoic Carbon Cycle: CO 2 and O 2 : 1155–1156 p.

Howell, D., Stachel, T., Stern, R. A., Pearson, D. G., Nestola, F., Hardman, M. F., Harris, J. W., Jaques, A. L., Shirey, S. B., Cartigny, P., Smit, K. V., Aulbach, S., Brenker, F. E., Jacob, D. E., and others, 2020, Deep carbon through time: Earth's diamond record and its implications for carbon cycling and fluid speciation in the mantle: Geochimica et Cosmochimica Acta, v. 275, p. 99–122.

Ickert, R. B., Stachel, T., Stern, R. A., and Harris, J. W., 2015, Extreme 18O-enrichment in majorite constrains a crustal origin of transition zone diamonds: Geochemical Perspectives Letters, v. 1, p. 65–74.

Jaisi, D. P., and Blake, R. E., 2010, Tracing sources and cycling of phosphorus in Peru Margin sediments using oxygen isotopes in authigenic and detrital phosphates: Geochimica et Cosmochimica Acta, v. 74, p. 3199–3212.

Johnston, D. T., MacDonald, F. A., Gill, B. C., Hoffman, P. F., and Schrag, D. P., 2012, Uncovering the neoproterozoic carbon cycle: Nature, v. 483, p. 320–323.

Kasting, J. F., and Canfield, D. E., 2012, The Global Oxygen Cycle: Fundamentals of Geobiology, p. 93–104.

Katsev, S., and Crowe, S. A., 2015, Organic carbon burial efficiencies in sediments: The power law of mineralization revisited: GEOLOGY, v. 43.

Kipp, M. A., and Stüeken, E. E., 2017, Biomass recycling and Earth's early phosphorus cycle: Science Advances, v. 3, p. 1–7.

Korenaga, J., 2013, Initiation and Evolution of Plate Tectonics on Earth: Theories and Observations: Annual Review of Earth and Planetary Sciences, v. 41, p. 117–151.

Krissansen-Totton, J., Buick, R., and Catling, D. C., 2015, A statistical analysis of the carbon isotope record from the Archean to phanerozoic and implications for the rise of oxygen: American Journal of Science, v. 315, p. 275–316.

Kump, L. R., 2008, The rise of atmospheric oxygen: Nature, v. 451, p. 277–278.

Kump, L. R., and Arthur, M. A., 1999, Interpreting carbon-isotope excursions: Carbonates and organic matter: Chemical Geology, v. 161, p. 181–198.

Laakso, T. A., and Schrag, D. P., 2014, Regulation of atmospheric oxygen during the Proterozoic: Earth and Planetary Science Letters, v. 388, p. 81–91.

Larsen, I. J., Almond, P. C., Eger, A., Stone, J. O., Montgomery, D. R., and Malcolm, B., 2014a, Rapid soil production and weathering in the Southern Alps, New Zealand: Science, v. 343, p. 637–640.

Larsen, I. J., Montgomery, D. R., and Greenberg, H. M., 2014b, The contribution of mountains to global denudation: Geology, v. 42, p. 527–530.

Lasaga, A. C., and Ohmoto, H., 2002, The oxygen geochemical cycle: Dynamics and stability: Geochimica et Cosmochimica Acta, v. 66, p. 361–381.

Laurenceau‐Cornec, E. C., Le Moigne, F. A. C., Gallinari, M., Moriceau, B., Toullec, J., Iversen, M. H., Engel, A., and De La Rocha, C. L., 2019, New guidelines for the application of Stokes' models to the sinking velocity of marine aggregates: Limnology and Oceanography, p. lno.11388.

Lenton, T. M., Boyle, R. A., Poulton, S. W., Shields-Zhou, G. A., and Butterfield, N. J., 2014, Co-evolution of eukaryotes and ocean oxygenation in the Neoproterozoic era: Nature Geoscience, v. 7, p. 257–265.

Li, C., Planavsky, N. J., Love, G. D., Reinhard, C. T., Hardisty, D., Feng, L., Bates, S. M., Huang, J., Zhang, Q., Chu, X., and Lyons, T. W., 2015, Marine redox conditions in the middle Proterozoic ocean and isotopic constraints on authigenic carbonate formation: Insights from the Chuanlinggou Formation, Yanshan Basin, North China: Geochimica et Cosmochimica Acta, v. 150, p. 90–105.

Liu, P., Liu, J., Ji, A., Reinhard, C. T., Planavsky, N. J., Babikov, D., Najjar, R. G., and Kasting, J. F., 2021, Triple oxygen isotope constraints on atmospheric O2 and biological productivity during the mid-Proterozoic.: Proceedings of the National Academy of Sciences of the United States of America, v. 118.

Lyons, T. W., Reinhard, C. T., and Planavsky, N. J., 2014, The rise of oxygen in Earth's early ocean and atmosphere: Nature, v. 506, p. 307–315.

Marais, D. J. D., Strauss, H., Summons, R. E., and Hayes, J. M., 1992, Carbon isotope evidence for the stepwise oxidation of the Proterozoic environment: Nature, v. 359, p. 605–609.

Marshall, A. O., Corsetti, F. A., Sessions, A. L., and Marshall, C. P., 2009, Raman spectroscopy and biomarker analysis reveal multiple carbon inputs to a Precambrian glacial sediment: Organic Geochemistry, v. 40, p. 1115–1123.

McDonnell, A. M. P., and Buesseler, K. O., 2010, Variability in the average sinking velocity of marine particles: Limnology and Oceanography, v. 55, p. 2085–2096.

Middelburg, J. J., 1989, A simple rate model for organic matter decomposition in marine sediments: Geochimica et Cosmochimica Acta, v. 53, p. 1577–1581.

Milliman, J. D., and Meade, R. H., 1983, World-wide delivery of sediment to the oceans.: Journal of Geology, v. 91, p. 1–21.

Miyazaki, Y., Planavsky, N. J., Bolton, E. W., and Reinhard, C. T., 2018, Making Sense of Massive Carbon Isotope Excursions With an Inverse Carbon Cycle Model: Journal of Geophysical Research: Biogeosciences, v. 123, p. 2485–2496.

Och, L. M., and Shields-Zhou, G. A., 2012, The Neoproterozoic oxygenation event: Environmental perturbations and biogeochemical cycling: Earth-Science Reviews, v. 110, p. 26–57.

Planavsky, N. J., Cole, D. B., Isson, T. T., Reinhard, C. T., Crockford, P. W., Sheldon, N. D., and Lyons, T. W., 2018, A case for low atmospheric oxygen levels during Earth's middle history: Emerging Topics in Life Sciences, v. 2, p. 149–159.

Planavsky, N. J., Reinhard, C. T., Wang, X., Thomson, D., McGoldrick, P., Rainbird, R. H., Johnson, T., Fischer, W. W., and Lyons, T. W., 2014, Low mid-proterozoic atmospheric oxygen levels and the delayed rise of animals: Science, v. 346, p. 635–638.

Raiswell, R., and Berner, R. A., 1986, Pyrite and organic matter in Phanerozoic normal marine shales: Geochimica et Cosmochimica Acta, v. 50, p. 1967–1976.

Reinhard, C. T., Planavsky, N. J., Gill, B. C., Ozaki, K., Robbins, L. J., Lyons, T. W., Fischer, W. W., Wang, C., Cole, D. B., and Konhauser, K. O., 2017, Evolution of the global phosphorus cycle: v. 541, p. 386–389.

Reinhard, C. T., Planavsky, N. J., Robbins, L. J., Partin, C. A., Gill, B. C., Lalonde, S. V., Bekker, A., Konhauser, K. O., and Lyons, T. W., 2013, Proterozoic ocean redox and biogeochemical stasis: Proceedings of the National Academy of Sciences of the United States of America, v. 110, p. 5357–5362.

Schidlowski, M., 1988, A 3,800-million-year isotopic record of life from carbon in sedimentary rocks: Nature, v. 333, p. 313–318.

Schidlowski, M., 2001, Carbon isotopes as biogeochemical recorders of life over 3.8 Ga of earth history: Evolution of a concept: Precambrian Research, v. 106, p. 117–134.

Schidlowski, M., Eichmann, R., and Junge, C. E., 1976, Carbon isotope geochemistry of the Precambrian Lomagundi carbonate province, Rhodesia: Geochimica et Cosmochimica Acta, v. 40, p. 449–455.

Schrag, D. P., Higgins, J. A., Macdonald, F. A., and Johnston, D. T., 2013, Authigenic carbonate and the history of the global carbon cycle: Science, v. 339, p. 540–543.

Shen, Y., Knoll, A. H., and Walter, M. R., 2003, Evidence for low sulphate and anoxia in a mid-Proterozoic marine basin: Nature, v. 423, p. 632–635.

Sperling, E. A., Wolock, C. J., Morgan, A. S., Gill, B. C., Kunzmann, M., Halverson, G. P., Macdonald, F. A., Knoll, A. H., and Johnston, D. T., 2015, Statistical analysis of iron geochemical data suggests limited late Proterozoic oxygenation: Nature, v. 523, p. 451–454.

Stachel, T., Harris, J. W., and Muehlenbachs, K., 2009, Sources of carbon in inclusion bearing diamonds: Lithos, v. 112, p. 625–637.

Sun, X., and Turchyn, A. V., 2014, Significant contribution of authigenic carbonate to marine carbon burial: Nature Geoscience, v. 7, p. 201–204.

Tang, D., Shi, X., Wang, X., and Jiang, G., 2016, Extremely low oxygen concentration in mid-Proterozoic shallow seawaters: Precambrian Research, v. 276, p. 145–157.

Wallmann, K., and Aloisi, G., 2012, The Global Carbon Cycle: Geological Processes, in Fundamentals of Geobiology: John Wiley & Sons, Ltd, Chichester, UK, p. 20–35.

Willenbring, J. K., Codilean, A. T., and McElroy, B., 2013, Earth is (mostly) flat: Apportionment of the flux of continental sediment over millennial time scales: Geology, v. 41, p. 343–346.

Figure captions:

Fig. 1. (A) A compilation of carbonate carbon isotope values through time (data from Krissansen-Totton and others, 2015) and (B) a histogram and a probability distribution of the same data, illustrating a baseline carbonate $\delta^{13}C_{carb}$ value of ~0‰ throughout Earth's history.

Fig. 2. This cartoon represents some of the aspects of our modeling. The reactive transport models (RTMs) with grid points on the left are in regions of uplift and erosion. Ancient organic matter (OM) is uplifted in eroding soils in the vadose zone, where oxygen diffuses down causing OM oxidation. Our models typically use 400 grid points capturing the boundary layer of this oxidation (cf. Fig. 3). In our case, the 1D model in the oxidation zone is placed vertically. Denudation rates and OM content at depth are variable, so we model many different erosion rates and OM contents at depth (TOC_{init}), and then combine the results using probability distributions of each to estimate how much OM is oxidized. Different atmospheric oxygen levels are also used in the modeling. If ancient OM survives oxidation in the vadose zone, it is transported rapidly through the fluvial system to the ocean. A small portion of the OM may be oxidized in episodic overbank deposits. The 1D RTMs at the ocean bottom are for burial and diagenetic processes not modeled here. The results of the oxidative weathering model on the flux of organic carbon burial ($F_{b,org}$) were then used to calculate the net primary production, NPP = $F_{b,org}$ / ε, where ε is the fraction of organic matter that is not respired in the water column and buried in the sediment through sinking of organic particles.

Fig. 3. Examples depth dependent results for oxygen, OM, and pyrite at steady state for an erosion rate of 5 cm/kyr, a, TOC_{init} at depth of 0.75 wt. %. A. and B. show results for pO_2 of 1%PAL at two different pyrite amounts at depth (A. 0.2 wt.%, B. 0.4%). The pyrite remaining at the surface is significantly lower for the run with lower pyrite at depth than for more pyrite at depth, yielding pyr_{top} of 0.007%, vs. 0.054%, respectively. At this low pO_2, limited OM oxidation occurs, but the lower pyrite level at depth allows slightly more oxidation of OM (TOC_{top} of 0.713 vs. 0.723%). C. and D. contrast results for pO_2 10% PAL at depth for two different initial OM grain thicknesses. All simulations started with 10 micron OM thickness, except for 5 microns for part D. The larger surface areas of the numerous smaller grains (for a given TOC_{init}) in part D allows more OM oxidation due to the surface-area-dependent kinetics. Oxygen levels decay to zero at the bottom of the pyrite oxidation zone.

Fig. 4. Part A shows the ordinate (TOC_{top}) is the amount of TOC remaining at the surface for TOC at the bottom of the domain (TOC_{init}) of 0.75 (mass%), pyrite at the bottom of 0.4 (mass%), and an erosion rate of 5 cm/kyr, while part B shows the pyrite remaining at the surface. The small downward-pointing triangles for rate multiplier of 0.5 times the default rate, the circles are for the default rate, and the small upward pointing triangles a for rate multiplier of 2. More TOC and pyrite survives at the surface for the slower rates. Also shown for OM oxidation are cases with larger triangles for 0.1 and 10 times the default oxidation rate of OM. Pyrite survives at the surface only for relatively low pO_2. The rates for OM and pyrite oxidation were varied separately for the two figure parts, that is, in part A the pyrite kinetics were the default rates and in part B the OM oxidation rates were the default values.

Fig. 5. TOC_{top} contoured vs. pO_2 and TOC_{init} for various erosion rates (A. 2.5, B. 5.1, C. 10.1, D. 20.9 in cm/kyr). We include additional (unequally spaced) contours at 0.1, and 0.01, although these are not visible for all erosion rates. In part A, the rightmost contour line is for of 0.01. Parts of two of the contour lines were removed due to artifacts in the contouring scheme.

Fig. 6. Contours of *'used'* = (TOC_{init} -TOC_{top}) (in mass%) as a function of pO_2 and TOC_{init} for various erosion rates (A. 2.5, B. 5.1, C. 10.1, D. 20.9 in cm/kyr).

Fig. 7. δ_w' values calculated from the expected values of *'used'* based on specific erosion rates (A. 2.5, B. 5.1, C. 10.1, D. 20.9 in cm/kyr), contoured versus pO_2 and <TOC_{init}> (the expected value of TOC_{init} from the beta distributions).

Fig. 8. The organic matter burial flux relative to total burial ($f_{b,org}$) calculated from the expected values of *'used'* based on specific erosion rates (A. 2.5, B. 5.1, C. 10.1, D. 20.9 in cm/kyr), contoured versus pO_2 and <TOC_{init}> (the expected value of TOC_{init} from the beta distributions).

Fig. 9. $F_{b,org}$ (in units of 10^{12} mol C/kyr) as a function of pO_2. Part A is for no overbank oxidation, while parts B and C are for 1000 and 10,000 years of overbank oxidation, respectively. Thick curves correspond to <er> of 9.35 and 3.43 cm/kyr from Larsen-derived distributions, while thin curves are for <er> of 9.35 and 3.42 cm/kyr from beta distributions, with solid curves for the lower of the <er> choices and dashed curves for the higher <er> of the pairs. Each set has three curves corresponding to <TOC_{init}> of 0.50, 0.75 and 0.89 (mass%), with the higher value associated with the upper curves of each set.

Fig. 10. $F_{b,carb}$ (in units of 10^{12} mol C/kyr) as a function of pO_2. Part A is for no overbank oxidation, while parts B and C are for 1000 and 10,000 years of overbank oxidation, respectively. Thick curves correspond to <er> of 9.35 and 3.43 cm/kyr from Larsen-derived distributions, while thin curves are for <er> of 9.35 and 3.42 cm/kyr from beta distributions, with solid curves for the lower of the <er> choices and dashed curves for the higher <er> of the pairs. Each set has three curves corresponding to <TOC_{init}> of 0.50, 0.75 and 0.89 (mass%), with higher value associated with the upper curves of each set.

Fig. 11. $f_{b,org}$ as a function of pO_2. Part A is for no overbank oxidation, while parts B and C are for 1000 and 10,000 years of overbank oxidation, respectively. Thick curves correspond to <er> of 9.35 and 3.43 cm/kyr from Larsen-derived distributions, while thin curves are for <er> of 9.35 and 3.42 cm/kyr from beta distributions, with solid curves for the lower of the <er> choices and dashed curves for the higher <er> of the pairs. Each set has three curves corresponding to <TOC_{init}> of 0.50, 0.75 and 0.89 (mass%), with higher value associated with the upper curves of each set. Canonical f_{org} values of 0.2 are only reached above pO_2 levels above 10-15% PAL with the higher erosion rates and higher values of <TOC_{init}>.

Fig. 12. Δ_B (part A) and $\delta_{b,carb}$ (part B) as a function of time from Krissansen-Totton and others (2015). Δ_B was derived from $\delta_{b,org}$ and $\delta_{b,carb}$ measurements in sediments. Both curves involve LOWESS smoothing of measured data. See Table A4 for definitions.

Fig. 13. $f_{b,org}$ as a function of time. The mean TOC_{init} value was assumed to be 0.75%. For the age range of 0-800 Ma we show results assuming all OM is oxidized (solid curves) and pO_2 = 18% PAL (dashed curves). For the age range of 810-2500 Ma we show results for pO_2 = 4.98% PAL (solid curves) and pO_2 = 0.46% PAL (dashed curves). For the age range of 2510-4500 Ma we show results for pO_2 = 0.46% PAL (solid curves) and pO_2 = 0% PAL (dashed curves). The gray shading represents the 95% confidence intervals from Fig. 6 of Krissansen-Totton and others (2015). Part A-C show this relative burial flux for mean erosion rates of 3.427 cm/kyr (derived from the Larsen distribution), 3.516 cm/kyr (via the beta distribution), and 5.02 cm/kyr (via the beta distribution). The larger erosion rates are associated with larger values of $f_{b,org}$ for comparative cases. The 'all OM oxidized' curves are shown only for the mean erosion rates from the beta distributions. Parts A, B, and C, have respectively, 0, 1000 or 1000 years of overbank oxidation. Part D shows curves for each assumed oxygen le noted above for <er>=5.02 cm/kyr at each of the overbank choices (0, 1000 or 1000 years of overbank oxidation), except that is, not relevant for the pO_2 = 0% PAL case. Part E shows results for each oxygen level, <er>=5.02 cm/kyr, and 1000 years of overbank oxidation. For this partvel we vary $F_{w,carb}$, including the default value of 34,000 x10^{12} mol C/kyr (as used in the other figure parts), and also show results for half, double, and ten times that default

value. Part F shows the effect of variation in the exposed land surface area (SA_{land}). The default value of SA_{land} used above is 1.48×10^{14} m^2. In this figure part we show how $f_{b,org}$ varies for the default SA_{land}, as well as setting that to half its default value, for each oxygen level, <er>=5.02 cm/kyr, 1000 years of overbank oxidation, and the default $F_{w,carb}$. This last figure part does not include SA_{land} variations for the age range 2510-4500 Ma.

Fig. 14. $F_{b,org}$ (in units of 10^{12} mol C/kyr) as a function of time using the same scheme as the parts in Fig. 13 (except without the confidence limits). Note the different ordinate scales for part E.

Fig. 15. Burial efficiency of marine biological pump in major geologic times of Archean, GOE/Lomagundi, Mid-proterozoic, and Phanerozoic. Results are from stochastic simulation of the 1D model under four different atmospheric oxygen scenarios (Lyons and others, 2014). Due to low rate of organic matter degradation under anoxic conditions (Katsev and Crowe, 2015), burial efficiency in the Archean oceans is high and it decreases to the modern values (<1%) as the oceans become more oxygenated.

Fig. 16. Ocean-atmosphere oxygen concentration and marine net primary production (NPP) through time. Grey shapes and lines, respectively, correspond to the most probable range (±σ) and the average value of NPP through time, resulted from stochastic modeling (equation 3). The arrows for the NPP range during the GOE and Phanerozoic indicate standard deviation values larger than 1000 Tmol/year. The strength of marine NPP is mainly controlled by the efficiency of the carbon pump (Figure. 15), and organic matter oxidation in terrestrial systems. Well-oxygenated ocean-atmosphere systems promote enhanced oxidation of organic matter on lands and efficient nutrient cycling in the ocean (Kipp and Stüeken, 2017) (low burial efficiency), both of which would reflect an elevation in the marine NPP (equation 3).

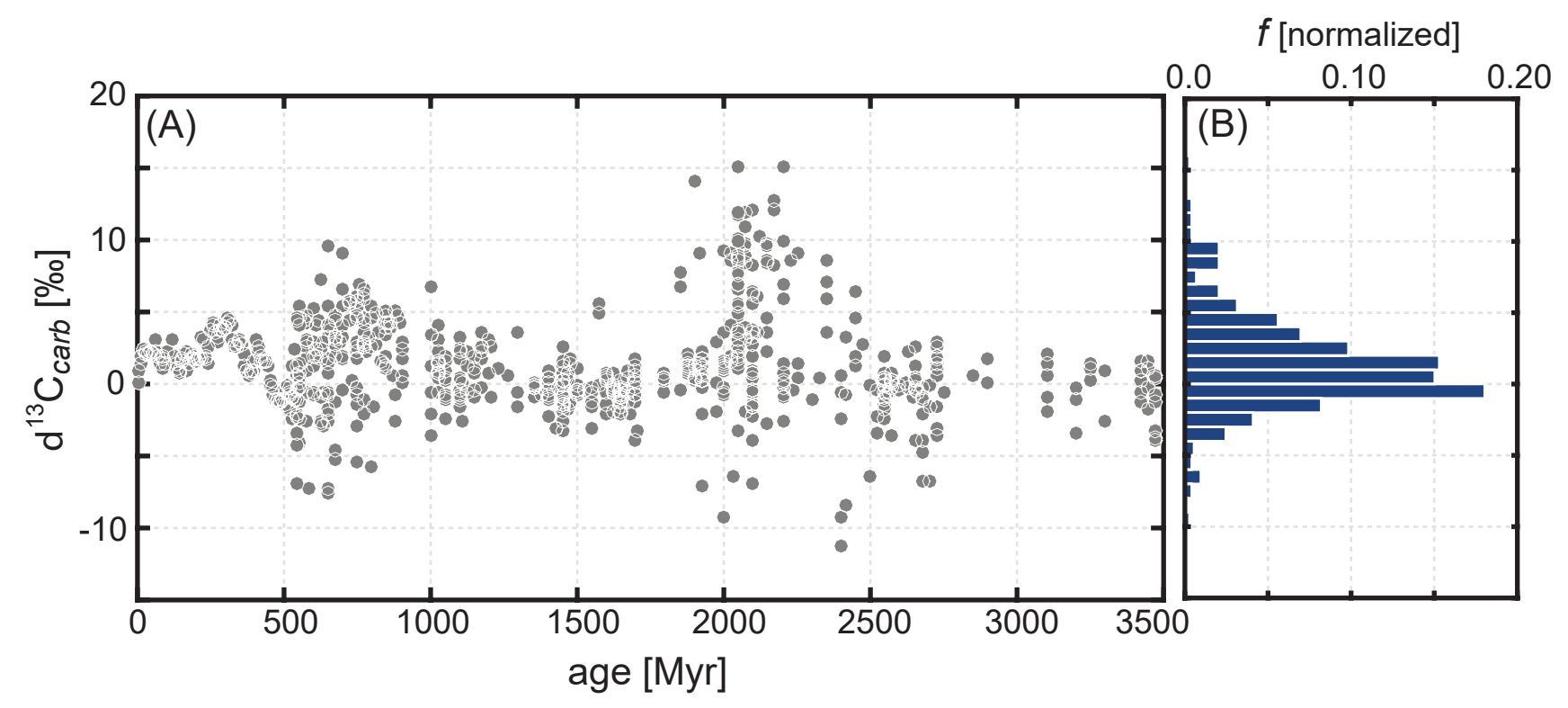
(A)
(B)
20
10
0
-10
0
500
1000
1500
2000
2500
3000
3500
age [Myr]
d13Ccarb [‰]
f [normalized]
0.0
0.10
0.20

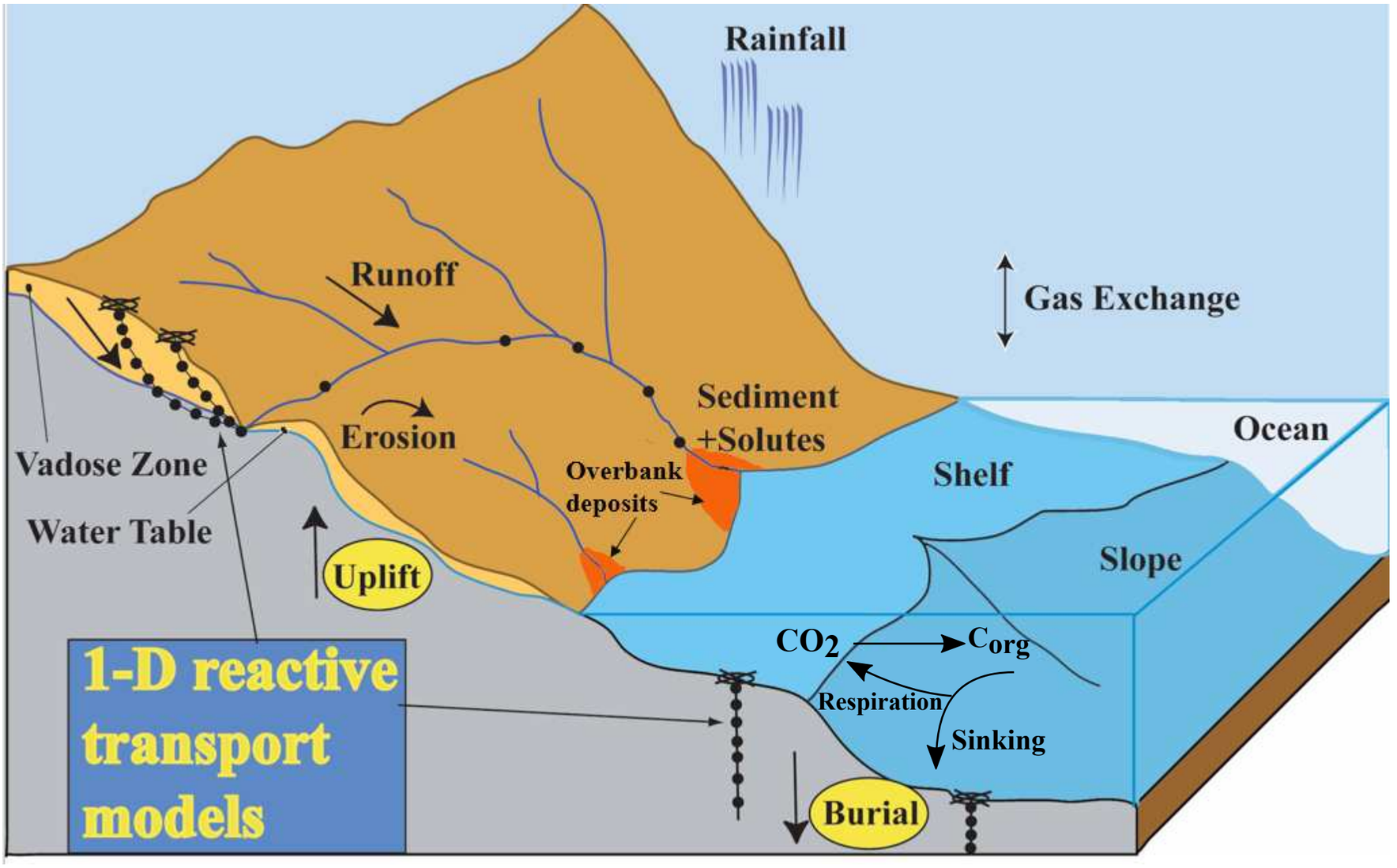
Rainfall
Runoff
Gas Exchange
Sediment
+Solutes
Erosion
Ocean
Vadose Zone
Overbank
deposits
Shelf
Water Table
Uplift
Slope
CO_2
C_{org}
Respiration
Sinking
1-D reactive
transport
models
Burial

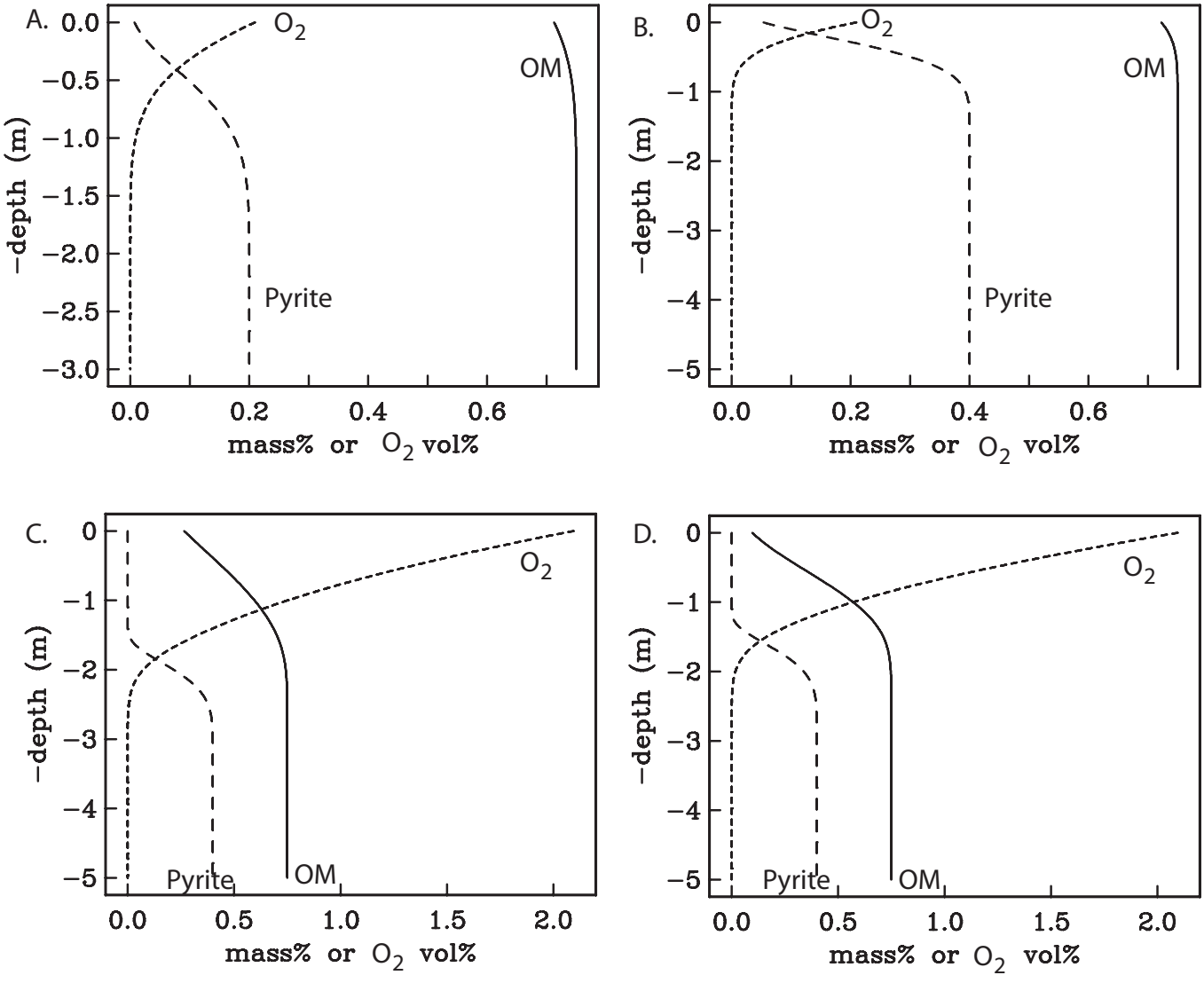
A.
B.
C.
D.
O2
OM
Pyrite
−depth (m)
mass% or O2 vol%
0.0
0.2
0.4
0.6
0.5
1.0
1.5
2.0
0
−0.5
−1.0
−1.5
−2.0
−2.5
−3.0
−1
−2
−3
−4
−5

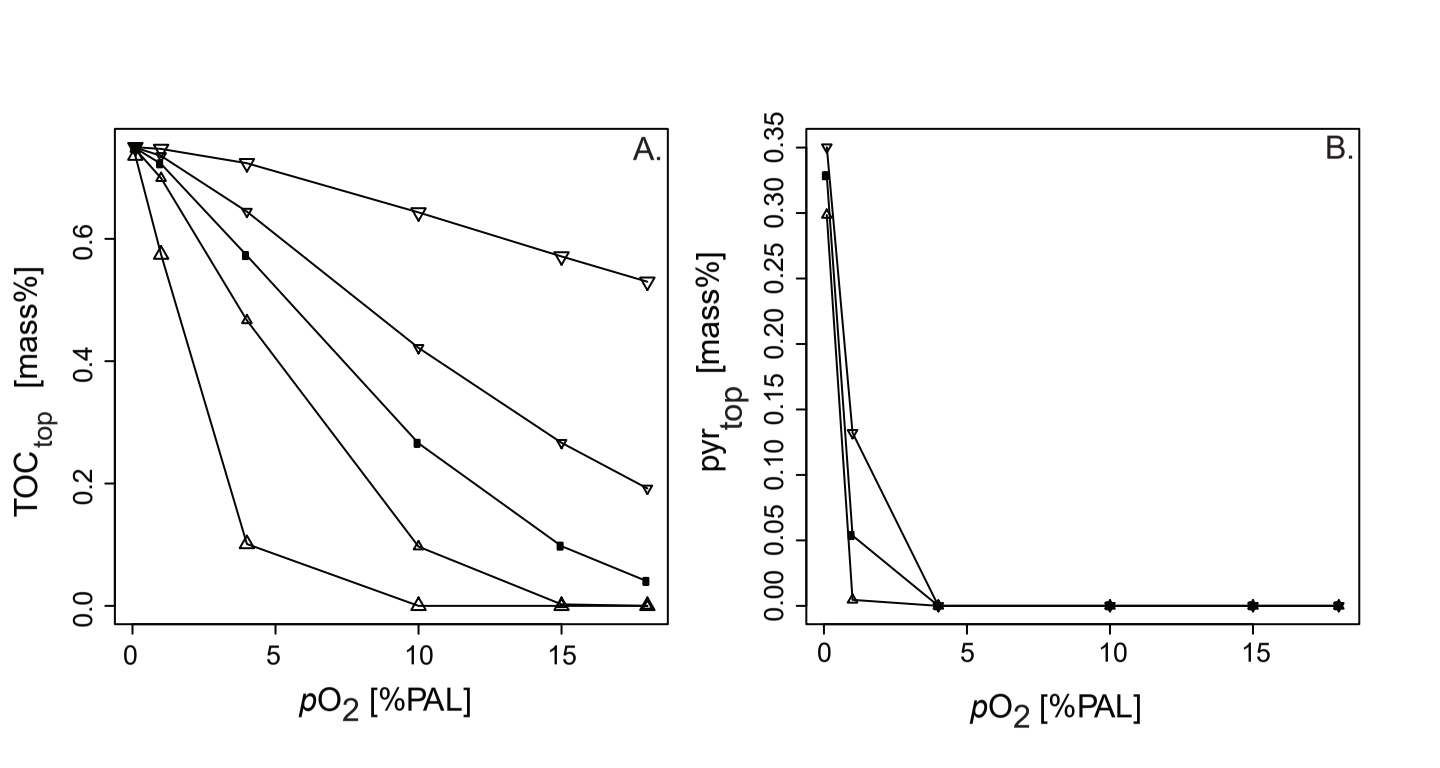
A.
TOC$_{top}$ [mass%]
0.0
0.2
0.4
0.6
0
5
10
15
pO_2 [%PAL]
B.
pyr$_{top}$ [mass%]
0.00
0.05
0.10
0.15
0.20
0.25
0.30
0.35
0
5
10
15
pO_2 [%PAL]

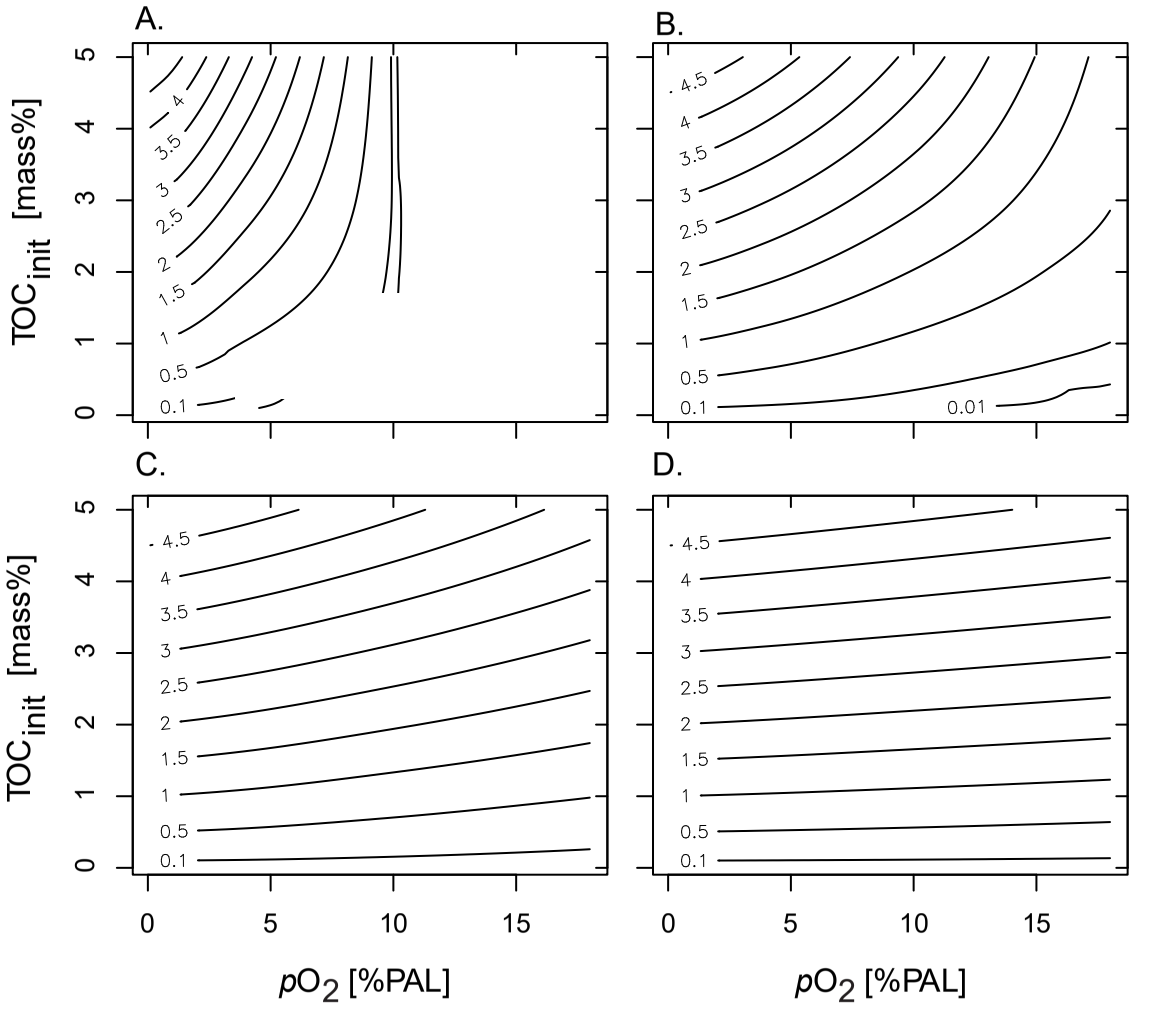
A.
B.
C.
D.
TOC$_{init}$ [mass%]
pO_2 [%PAL]
0
5
10
15
0.1
0.5
1
1.5
2
2.5
3
3.5
4
4.5
0.01

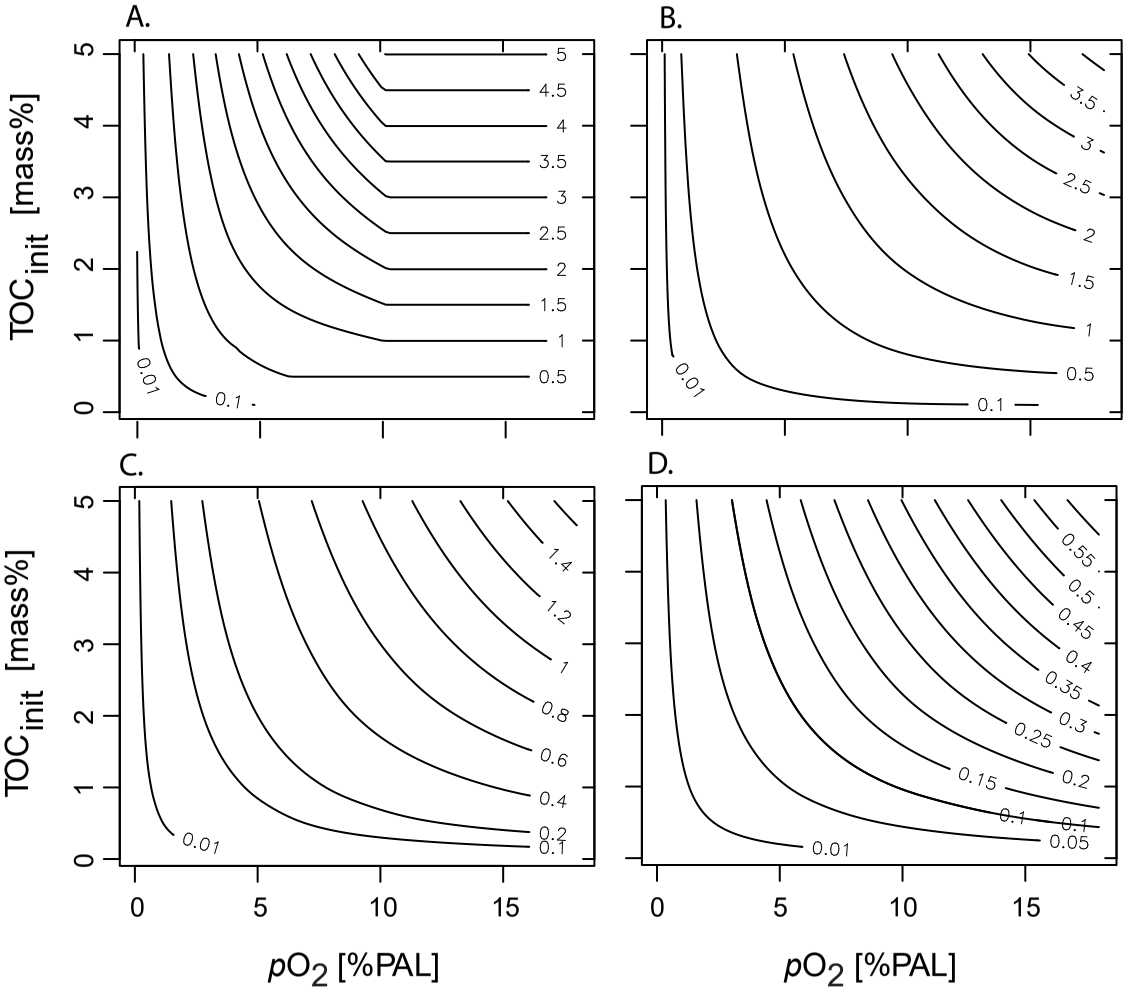
A.
B.
C.
D.
TOC$_{init}$ [mass%]
pO_2 [%PAL]
0
5
10
15
0.01
0.1
0.5
1
1.5
2
2.5
3
3.5
4
4.5
5
0.2
0.4
0.6
0.8
1.2
1.4
0.05
0.15
0.25
0.3
0.35
0.45
0.55

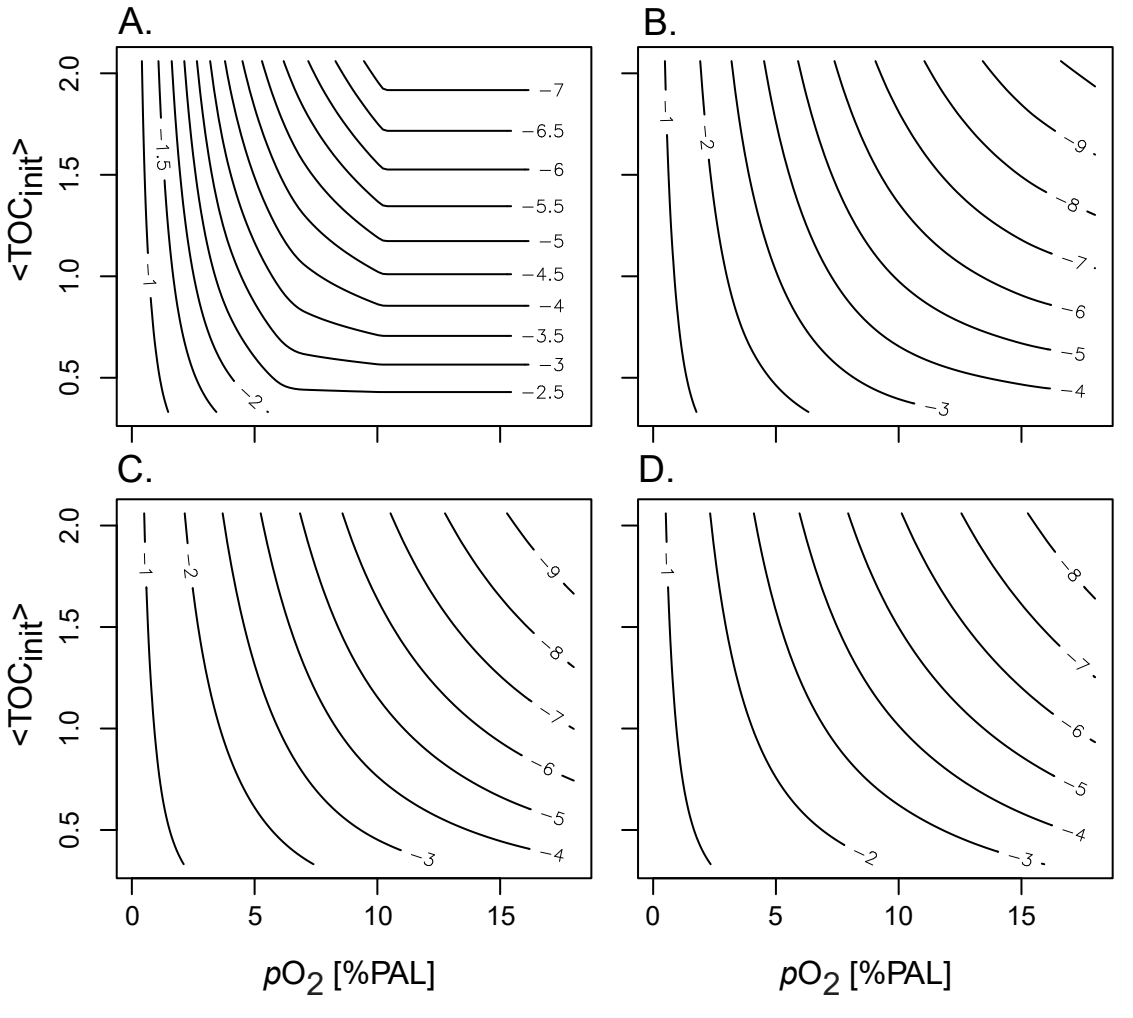
A.
B.
C.
D.
<TOC_init>
0.5
1.0
1.5
2.0
0
5
10
15
pO2 [%PAL]
−1
−1.5
−2
−2.5
−3
−3.5
−4
−4.5
−5
−5.5
−6
−6.5
−7
−8
−9

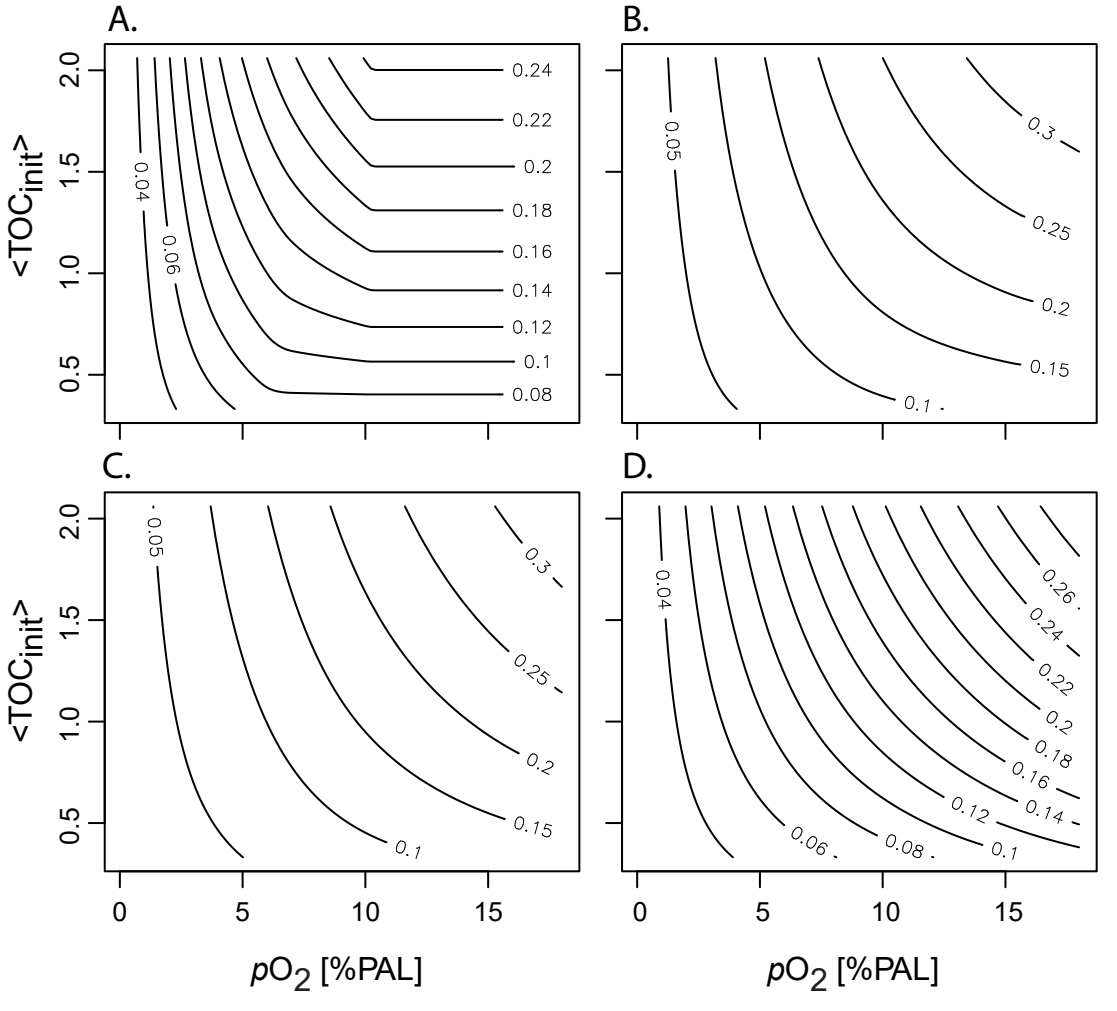
A.
B.
C.
D.
<TOC_init>
<TOC_init>
0.5
1.0
1.5
2.0
0
5
10
15
pO2 [%PAL]
pO2 [%PAL]
0.24
0.22
0.2
0.18
0.16
0.14
0.12
0.1
0.08
0.04
0.06
0.05
0.3
0.25
0.2
0.15
0.1
0.05
0.3
0.25
0.2
0.15
0.1
0.04
0.26
0.24
0.22
0.2
0.18
0.16
0.14
0.12
0.1
0.08
0.06

A.
B.
C.
$F_{b,org}$
0
2000
4000
6000
8000
10000
12000
15000
20000
pO_2 [%PAL]
0.1
1
10
20

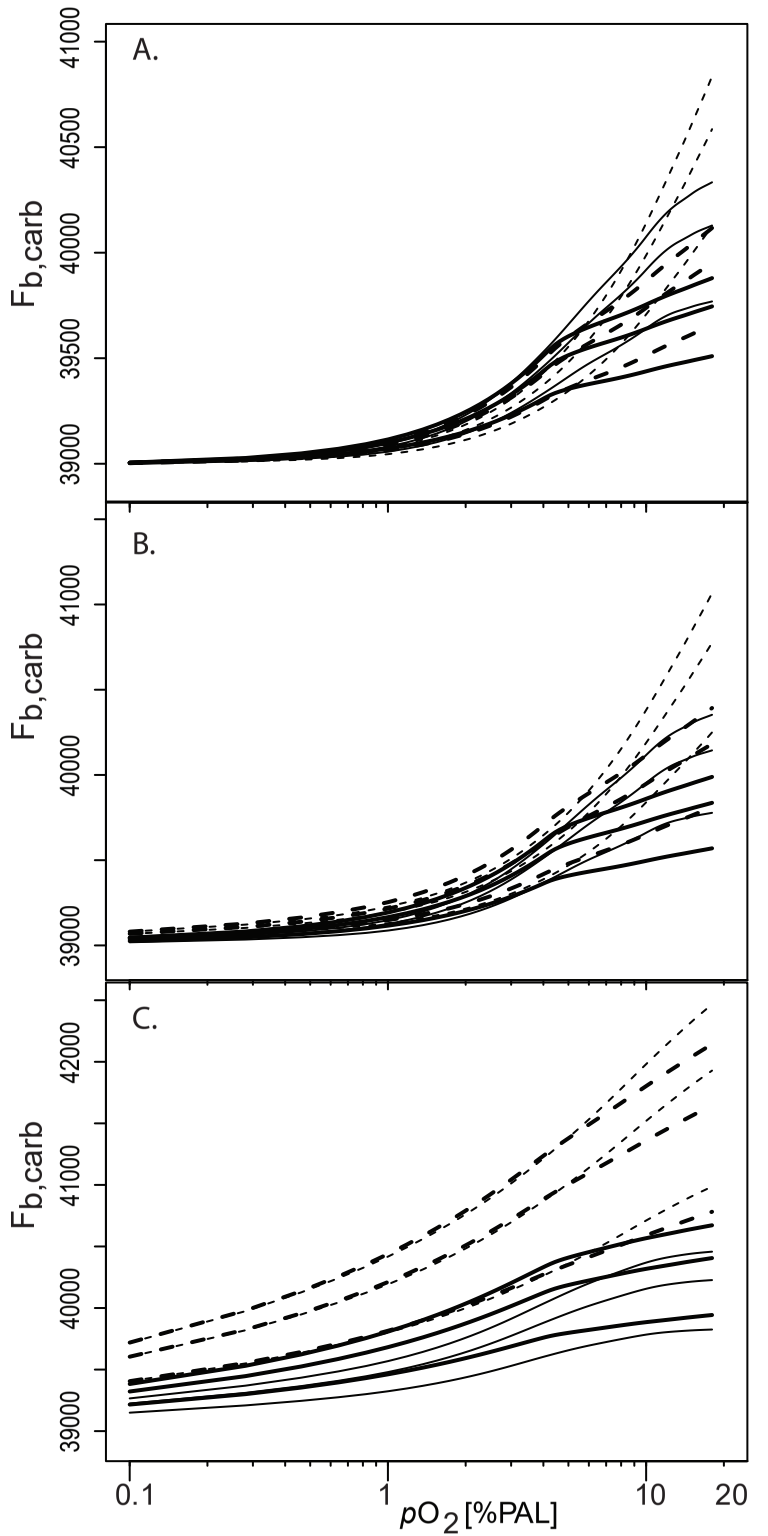
A.
B.
C.
$F_{b,carb}$
39000
39500
40000
40500
41000
42000
0.1
1
10
20
pO_2 [%PAL]

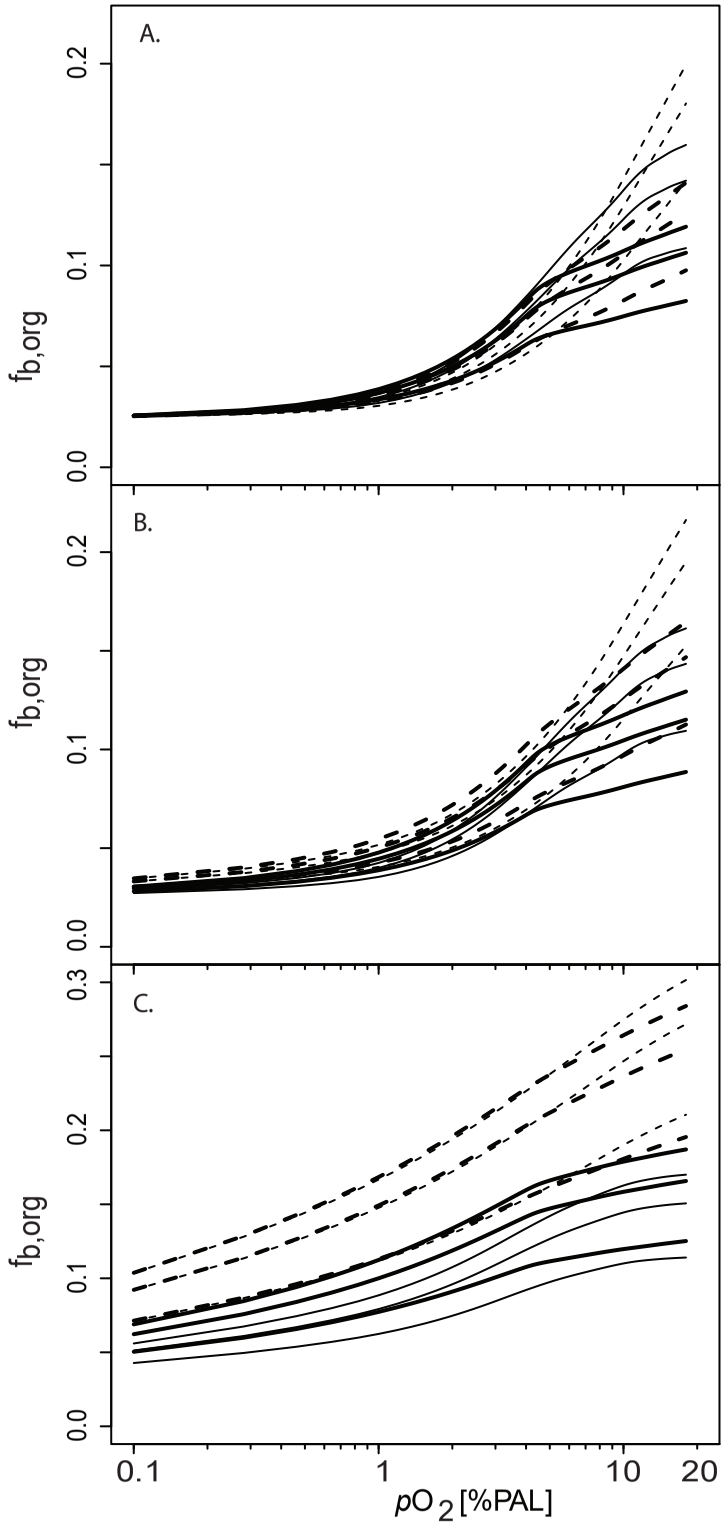
A.
B.
C.
$f_{b,org}$
0.0
0.1
0.2
0.3
0.1
1
10
20
pO_2 [%PAL]

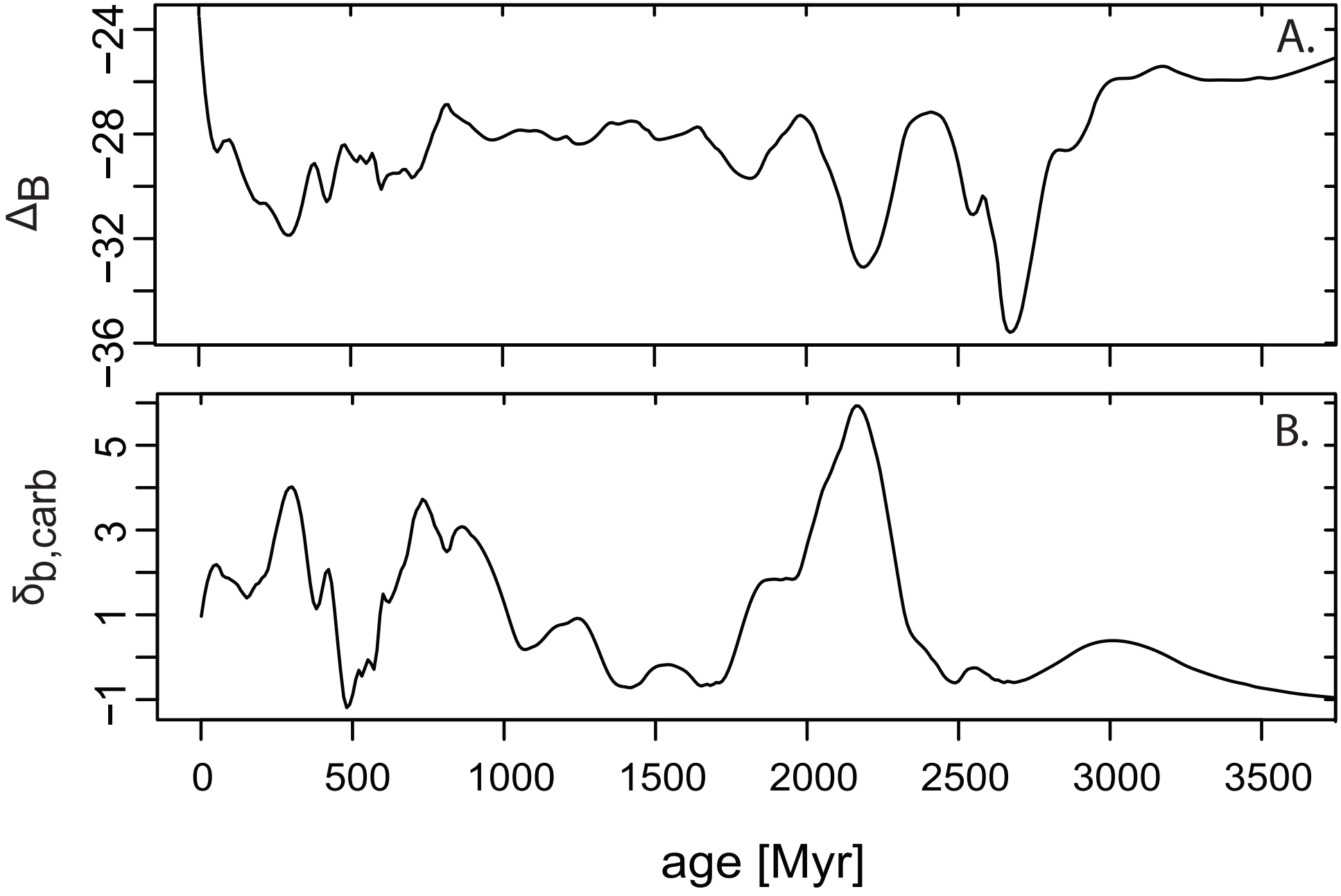
A.
B.
Δ_B
$\delta_{b,carb}$
−24
−28
−32
−36
5
3
1
−1
0
500
1000
1500
2000
2500
3000
3500
age [Myr]

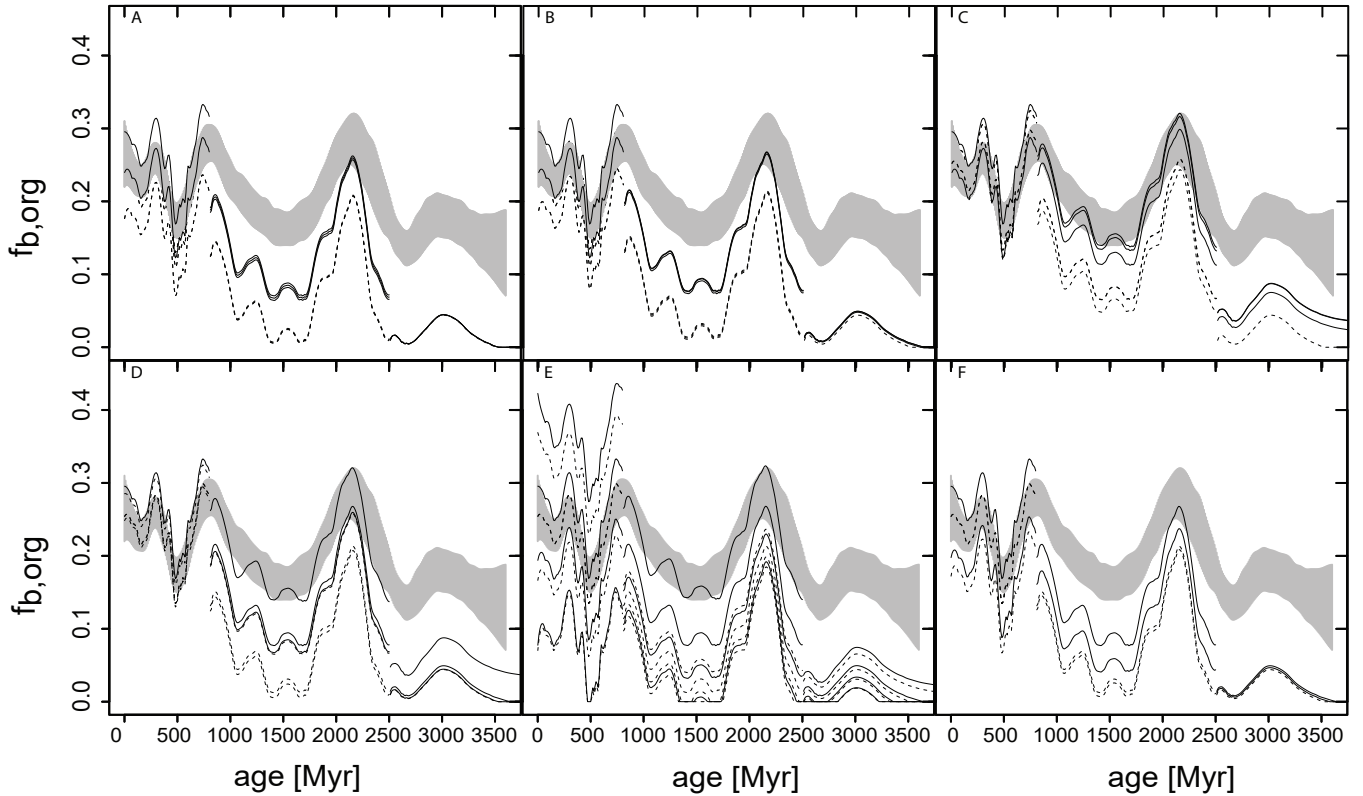
A
B
C
D
E
F
$f_{b,org}$
$f_{b,org}$
0.0
0.1
0.2
0.3
0.4
0
500
1000
1500
2000
2500
3000
3500
age [Myr]
age [Myr]
age [Myr]

A
B
C
D
E
F
$F_{b,org}$
$F_{b,org}$
0
5000
10000
15000
20000
40000
60000
0
500
1000
1500
2000
2500
3000
3500
age [Myr]
age [Myr]
age [Myr]

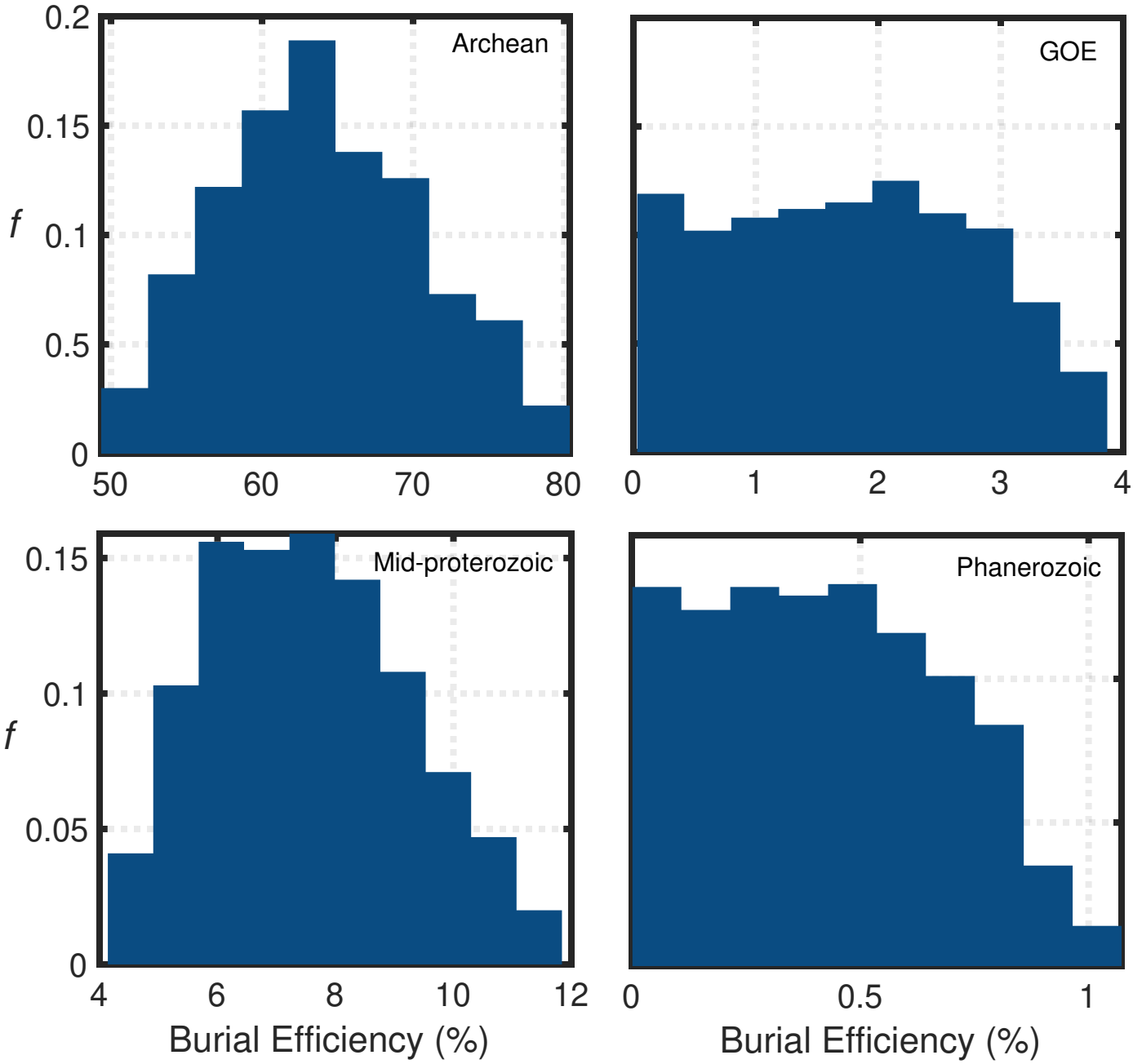
Archean
GOE
Mid-proterozoic
Phanerozoic
f
f
0.2
0.15
0.1
0.5
0
50
60
70
80
0
1
2
3
4
0.15
0.1
0.05
0
4
6
8
10
12
0
0.5
1
Burial Efficiency (%)
Burial Efficiency (%)

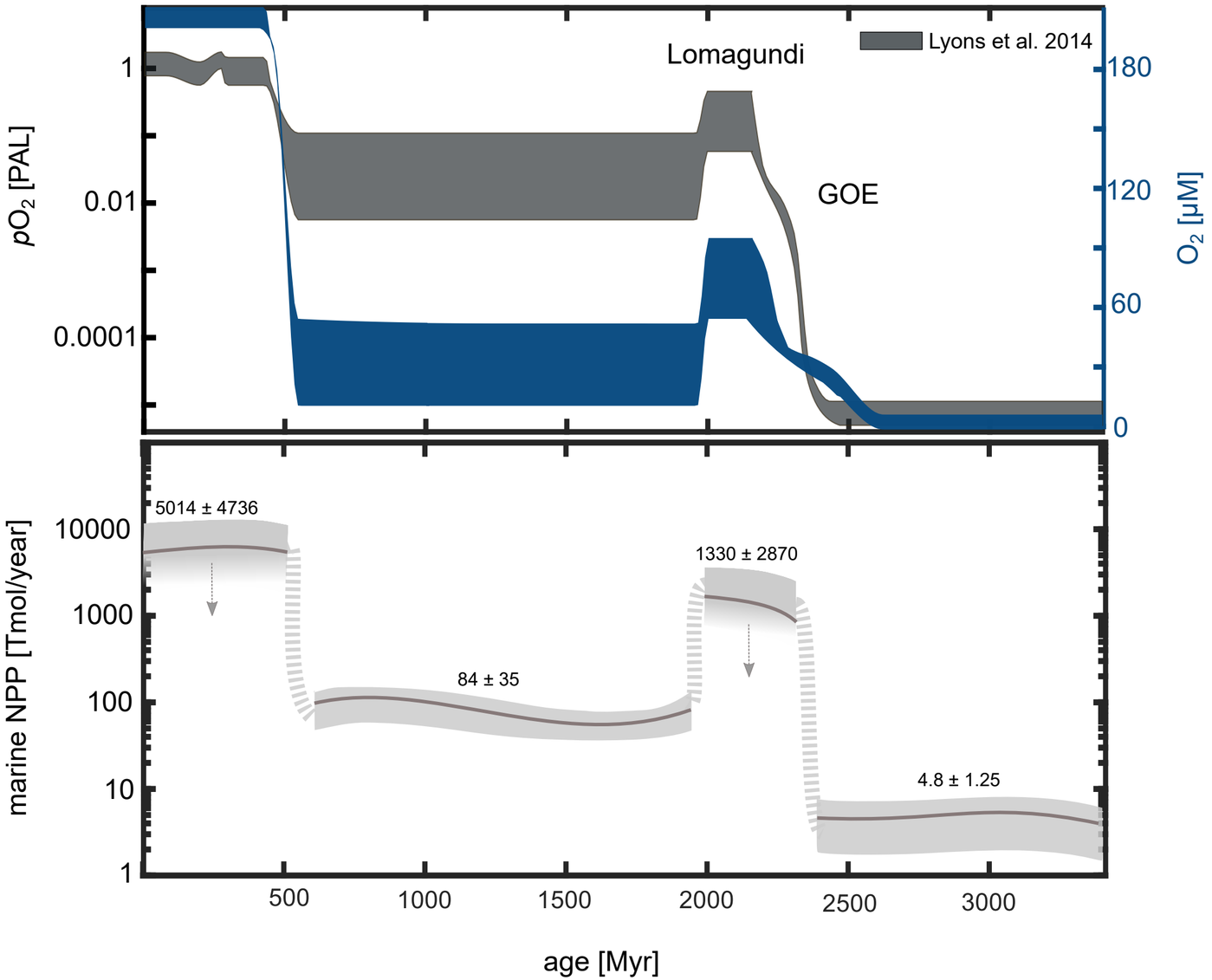
Lomagundi
Lyons et al. 2014
GOE
1
0.01
0.0001
pO2 [PAL]
180
120
60
0
O2 [µM]
5014 ± 4736
1330 ± 2870
84 ± 35
4.8 ± 1.25
10000
1000
100
10
1
marine NPP [Tmol/year]
500
1000
1500
2000
2500
3000
age [Myr]